Pergamon

Geochimica et Cosmochimica Acta, Vol. 65, No. 22, pp. 4155–4170, 2001

0016-7037/01 $20.00 + .00

PII S0016-7037(01)00700-1

Sorption of metal ions on clay minerals. III. Nucleation and epitaxial growth of Zn phyllosilicate on the edges of hectorite

MICHEL L. SCHLEGEL,[1,*,†] ALAIN MANCEAU,[1] LAURENT CHARLET,[1] DANIEL CHATEIGNER,[2] and JEAN-LOUIS HAZEMANN[1,3]

[1]Environmental Geochemistry Group, LGIT, Maison des Géosciences, Université J. Fourier and CNRS, BP 53 F-38041 Grenoble Cedex 9, France

[2]Laboratoire de Physique de l'État Condensé, Université du Maine, BP 535 F-72085 Le Mans Cedex 9, France

[3]Laboratoire de Cristallographie, CNRS, 25, avenue des Martyrs, BP 166 F-38042 Grenoble Cedex 9, France

(*Received September* 21, 2000; *accepted in revised form April* 25, 2001)

Abstract—The impact of dissolved Si ($[Si]_{aq}$) on Zn uptake in dilute suspensions (0.65 g/L) of hectorite was investigated at pH 7.30, a total Zn concentration (TotZn) of 520 μM, and ionic strength of 0.3 M ($NaNO_3$ salt) by kinetics experiments and polarized extended X-ray absorption fine structure (P-EXAFS) spectroscopy.

At low $[Si]_{aq}$ (~30 to 60 μM), 5.8% of TotZn was adsorbed within the first 3 h of reaction. The sorption rate was lower afterwards, and Zn uptake amounted to 14.6% of TotZn after 168 h of reaction. These rates are consistent with Zn sorption on pH-dependent edge sites of hectorite platelets. At high $[Si]_{aq}$ (~530 μM), a higher initial sorption rate was observed, the fraction of Zn removed amounting to 15.2% of TotZn at t = 3 h and 90.7% at t = 120 h. After 9 h of reaction time, Si uptake also occurred; the Si/Zn uptake ratio (1.09 ± 0.08) was between those of TO (~0.67) and TOT (~1.33) trioctahedral phyllosilicates, which suggests the neoformation of a Zn phyllosilicate. In the absence of hectorite, neither Zn nor Si were removed from solution, even at high $[Si]_{aq}$, indicating that Zn uptake occurred by sorption on hectorite surface.

Comparison of spectra for sorption samples and Zn references indicated that sorbed Zn was located in a clay-like structural environment. The angular dependence observed for all P-EXAFS spectra demonstrated that Zn cations are structurally attached to the edges of hectorite platelets. The size and structure of these Zn surface complexes varied with $[Si]_{aq}$ and reaction time. At low $[Si]_{aq}$ and after a long reaction time (t = 96 h), Zn was surrounded by in-plane 1.7 ± 0.6 Zn and 1.4 ± 0.3 Mg at 3.08 Å, and by out-of-plane 0.6 ± 1.1 Si at 3.28 Å. These results point to predominant formation of small polymers containing on average two to three Zn cations and located in structural continuity with the hectorite octahedral sheet. At high $[Si]_{aq}$, higher numbers of Zn and Si and lower numbers of Mg neighbors were detected at t = 9 h; at t = 120 h, Zn was surrounded by in-plane 6.0 ± 0.4 Zn at 3.10 Å and by out-of-plane 3.6 ± 0.4 Si at 3.27 Å as in a Zn phyllosilicate. These results document for the first time the nucleation and epitaxial growth at ambient temperature of Zn phyllosilicate at the edges of smectite minerals under controlled laboratory conditions. *Copyright © 2001 Elsevier Science Ltd*

1. INTRODUCTION

Silicon is one of the most widespread chemical elements at Earth's surface. Concentrations of silicic acid in terrestrial waters typically range between 10 and 80 ppm (Davies and De Wiest, 1966) and are controlled by dissolution of rock-forming silicates (Drever, 1997; Rimstidt, 1997) and dissolution-precipitation of secondary phases, including phyllosilicates. Heterogeneous nucleation of clay minerals is commonly observed, and these solid phases can grow on detrital or secondary phyllosilicates (Nagy et al., 1999), on dissimilar phases such as quartz (Davis et al., 1998), volcanic glass (Banfield et al., 1991), and even organic matter (Fortin et al., 1997). Because these neoformation reactions significantly affect the cycling of major and trace cationic elements in soils and weathering profiles (Harder, 1977; Righi and Meunier, 1995; Drever, 1997; Manceau et al., 2000), characterization of the mechanisms by which phyllosilicates nucleate and grow at mineral–water interfaces is warranted.

Recent microscopic and spectroscopic laboratory studies of cation sorption on silicate minerals reported the neoformation of pure and mixed hydroxide phases, e.g., layered double hydroxides (O'Day et al., 1994a, 1996; Farquhar et al., 1996; Papelis and Hayes, 1996; Scheidegger et al., 1996, 1997, 1998). Yet these compounds are seldom identified in natural systems. Formation of clay minerals on cation uptake in silica (Charlet and Manceau, 1994; Espinose de la Caillerie et al., 1995) and quartz suspensions (Manceau et al., 1999a) was documented by powder extended X-ray absorption fine structure (EXAFS) spectroscopy. However, the structural information obtained from powder EXAFS is limited to the immediate vicinity of the target atom, which hinders accurate characterization of the sorbate–sorbent structural relationship and therefore hampers discriminating between homogeneous and heterogeneous nucleation. Polarized EXAFS spectroscopy (P-EXAFS) of highly textured self-supporting films of fine-grained layer minerals can be used to overcome this limitation by disclosing the anisotropic environment of sorbate species structurally associated to sorbent phases (Manceau et al., 1998, 1999b). P-EXAFS was successfully applied by Schlegel et al. (1999a) to identify Co sorption sites in continuity with the octahedral sheets of hectorite, a magnesian smectite (Fig. 1). The EXAFS contribution from Mg cations of the octahedral sheet at R

* Author to whom correspondence should be addressed (Michel.Schlegel@colorado.edu).

† *Present address:* Department of Geological Sciences, University of Colorado, Boulder, CO 80309-0399, USA.

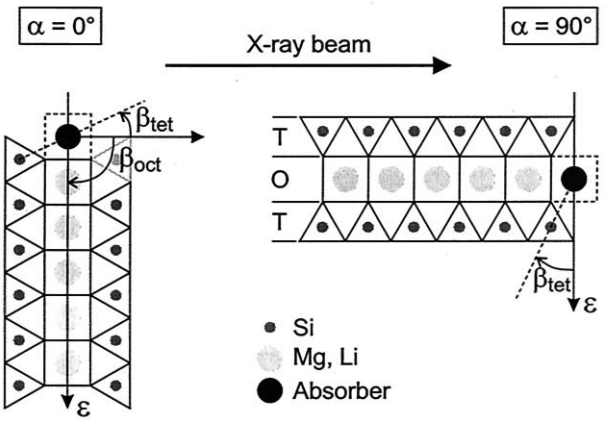

Fig. 1. Application of polarized EXAFS to the characterization of surface complexes located at the edges of phyllosilicate layers. Left: electric field vector ϵ parallel to the layer plane. Right: ϵ perpendicular to the layer plane. β_{oct}: angle between c^* and the vector connecting the sorbate to cations of the octahedral sheet. β_{tet}: angle between c^* and the vector connecting the sorbate to cations of the tetrahedral sheet.

~3.03 Å was enhanced for parallel orientation of the X-ray polarization vector and the phyllosilicate *ab* plane ($\alpha = 0$; Fig. 1, left) and extinguished for perpendicular orientation ($\alpha = 90°$; Fig. 1, right); whereas, the opposite polarization dependence was observed for the Si contribution. The ability of P-EXAFS to probe anisotropic coordination environments can be used to discriminate solids precipitated in bulk solutions, and thus having no peculiar orientation, from those formed in structural continuity with smectite layers. Both precipitation mechanisms lead to cation uptake, which refers to the partitioning of a dissolved species to a solid phase, regardless of the partitioning mechanism (Towle et al., 1997).

In this paper, P-EXAFS was used to study the mechanism of Zn sorption by hectorite at near-neutral pH. Emphasis was placed on the catalytic role of the sorbent surface and the importance of dissolved Si. The uptake of Zn and Si at pH 7.30 and solute silica representative of natural waters were measured. Zn phyllosilicate was identified by P-EXAFS and shown to be located in structural continuity with hectorite layers. Possible mechanisms of Zn phyllosilicate nucleation and growth on natural particles could then be identified; their impact on the fate of Zn in natural systems is discussed.

2. MATERIALS AND METHODS

2.1. Hectorite

Hectorite, $Na_{0.40}(Mg_{2.65}Li_{0.35})(Si_{3.95}Al_{0.05})O_{10}(OH)_2$ (SHCa-1), was purchased from the Source Clay Repository of the Clay Minerals Society. Raw clay weighing 10 g was dispersed in 500 mL of bidistilled water (Milli-Q). The < 2 μm fraction was isolated by centrifugation and treated several times with 10^{-4} M HNO_3-0.5 mol/L NaCl, then with a dithionite-citrate-bicarbonate solution for 1 h at pH 6.5, and finally with a 3% H_2O_2-0.5 mol/L NaCl solution for 1 h at 50°C (Schlegel et al., 1999a). The treated hectorite was repeatedly washed with a 0.3 mol/L $NaNO_3$ solution until no Cl^- could be detected by $AgNO_3$ testing, and stored as a 1.3 wt.% stock suspension at 4°C in the dark. The purified clay was characterized by X-ray diffraction on a Siemens D-5000 X-ray diffractometer. No crystallized carbonate mineral could be detected. The cation exchange capacity (CEC), measured by Cs exchange (Anderson and Sposito, 1991), is 840 meq kg^{-1}. Specific surface area determined by BET equals 114 m^2 g^{-1}.

2.2. Zn Uptake Experiments

All solutions were prepared with deionized water (Milli-Q) and chemicals of ACS reagent grade. Sorption experiments were conducted at 25 ± 0.1°C in thermostated polyethylene vessels. A rotating magnetic bar ensured stirring of the suspension, and an inert atmosphere was maintained by bubbling acid- and base-washed, water vapor-saturated Ar through the suspension (Schlegel et al., 1999a). A constant Na concentration of 0.3 mol/L was maintained using $NaNO_3$ (Fluka). pH measurements were performed with a combination electrode (Metrohm) calibrated with buffers (Merck, titrisol) and recalibrated at least every 48 h. Suspension pH values were adjusted by adding small aliquots of acidic (0.1 mol/L HNO_3-0.3 mol/L $NaNO_3$), basic (0.02 mol/L NaOH-0.28 mol/L $NaNO_3$), or basic silica (0.01 mol/L SiO_2-0.02 mol/L NaOH-0.28 mol/L $NaNO_3$) solutions, according to experimental conditions.

To assess the roles of dissolved Si and of the hectorite surface in Zn uptake, three experiments were performed by varying sorbent or silica concentrations. In the first (H30_SiZn), a dilute hectorite suspension (0.65 g L^{-1}) with a "high" solute Si concentration, $[Si]_{aq}$ ~530 μM, was prepared at pH 4 by mixing the hectorite stock suspension with acidic, basic silica, and $NaNO_3$ solutions. This suspension was allowed to react overnight without pH control before Zn addition. In the second (NoH_SiZn), a Si-enriched hectorite suspension was prepared similarly, allowed to react overnight, and then centrifuged to remove hectorite (30 min at 5000 rpm). A 100 mL aliquot of the sorbent-free supernatant was acidified with 50 μL of the acidic solution to limit contamination by atmospheric CO_2, filtered (Millipore 0.05 μm cellulose nitrate filter) to remove any remaining hectorite, poured back into a clean reaction vessel, and outgassed with humidified Ar for 1 h before Zn addition. Hence, NoH_SiZn differs from H30_SiZn only by the absence of hectorite particles. In the third (H30_Zn), a hectorite suspension (0.65 g L^{-1}) with a "low" $[Si]_{aq}$ (~30 to 60 μM) resulting from hectorite dissolution was prepared at pH 4 by mixing the hectorite stock suspension with only acidic and $NaNO_3$ solutions, and allowed to react overnight.

In all experiments, pH was adjusted to 7.30 before Zn addition. An aliquot of Zn solution (0.21 mol/L $Zn(NO_3)_2$-10^{-3} M HNO_3) was then added to obtain a total Zn concentration (TotZn) of 520 μM. The time of Zn addition is hereafter referred to as $t = 0$. Following Zn addition, pH was adjusted to 7.30 (± 0.05) within 2 h and kept at this value by adding basic silica (H30_SiZn and NoH_SiZn) or basic (H30_Zn) solutions at a slow rate (~50 μL min^{-1}) to avoid local supersaturation. At given times ($0 < t \leq 168$ h), 5 mL of a suspension was withdrawn from the reaction vessel with a plastic syringe connected to a polyeth-

Table 1. Samples analyzed by EXAFS spectroscopy.

Sample names	[hectorite] (g L^{-1})	Zn uptake[a] (%)	Γ^b (μmol g^{-1} hectorite)	$\frac{g\ Zn_{uptake}}{g\ hectorite}$ (%)	$[Si]_{aq}$ (μM)	Time (h)
H30_Zn_96h	0.65	11.4	91.1	0.57	51	96
H30_SiZn_9h	0.65	28.4	227	1.43	551	9
H30_SiZn_120h	0.65	90.7	725	4.56	544	120
NoH_SiZn_125h	0	0	/	/	572	125

[a] Initial Zn concentration TotZn = 520 μM.
[b] Ratio of the Zn uptake to the mass of hectorite.

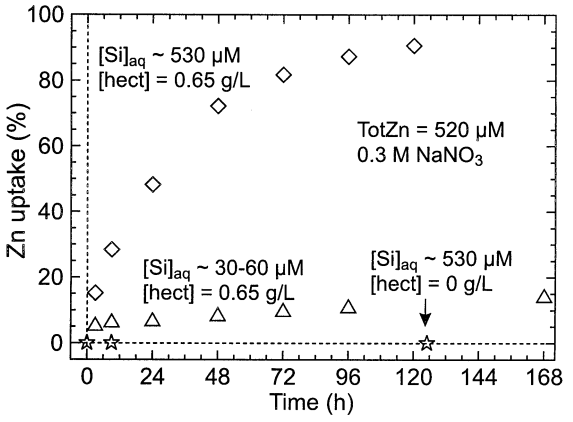

Fig. 2. Zn uptake as a function of initial $[Si]_{aq}$. TotZn = 520 μM at pH 7.30 for all experiments. The uncertainty in analytical measurement is smaller than the symbols. (◇): Solid concentration of hectorite [hect] = 0.65 g L^{-1}, $[Si]_{aq}$ ~530 μM, titration by 0.01 mol/L Na_2SiO_3-0.28 mol/L $NaNO_3$ (H30_SiZn). (△): [hect] = 0.65 g L^{-1}, $[Si]_{aq}$ ~30–60 μM, titration by 0.02 mol/L NaOH-0.28 mol/L $NaNO_3$ (H30_Zn); (☆): [hect] = 0 g L^{-1}, $[Si]_{aq}$ ~530 μM, titration by 0.01 mol/L Na_2SiO_3-0.28 mol/L $NaNO_3$ (NoH_SiZn).

ylene needle, centrifuged, and filtered (Millipore 0.05 μm cellulose nitrate filter). The first mL of the filtered supernatant was discarded to limit losses due to sorption on the filter. Filtered supernatants were acidified with ~50 μL of 0.1 mol/L HNO_3 and stored in the dark. Solute Zn, Si, and Mg concentrations in the filtered supernatant ($[Zn]_{aq}$, $[Si]_{aq}$, and $[Mg]_{aq}$) were measured by inductively coupled plasma-atomic emission spectrometry. $[Si]_{aq}$ never exceeded 600 μM. Therefore, silicic acid was undersaturated with respect to amorphous silica (solubility of ~2000 μM; Iler, 1979), and was assumed to remain predominantly in monomeric form (Stumm, 1992).

Zn uptake was determined from the difference between TotZn and $[Zn]_{aq}$, taking into account the dilution caused by addition of basic or basic silica solutions. The dilution factor for the i^{th} sample was calculated as

$$D_i = \prod_{j=1}^{i-1} \frac{v_j - v_{sample,j}}{v_j - v_{sample,j} + v_{b,j}}, \quad (1)$$

where v_j is the suspension volume before withdrawing the j^{th} sample, $v_{sample,j}$ is the volume of the j^{th} sample, and $v_{b,j}$ is the volume of basic or basic silica solution added after withdrawal of the j^{th} sample. D = 1 in the absence of dilution, and D = 0 for an infinite dilution. Calculations of D_i for H30_SiZn yielded D = 0.993 at t = 3 h and D = 0.952 at t = 120 h. Dilution was less important for H30_Zn (D = 0.996 at t = 168 h) and NoH_SiZn (D > 0.999 at t = 125 h). Speciation calculations at t = 0 showed that 98.3% of Zn in the supernatant was present as $Zn^{2+}_{(aq)}$, 1.3% as $ZnOH^{+}_{(aq)}$, and 0.4% as $Zn(OH)_{2(aq)}$ (Baes and

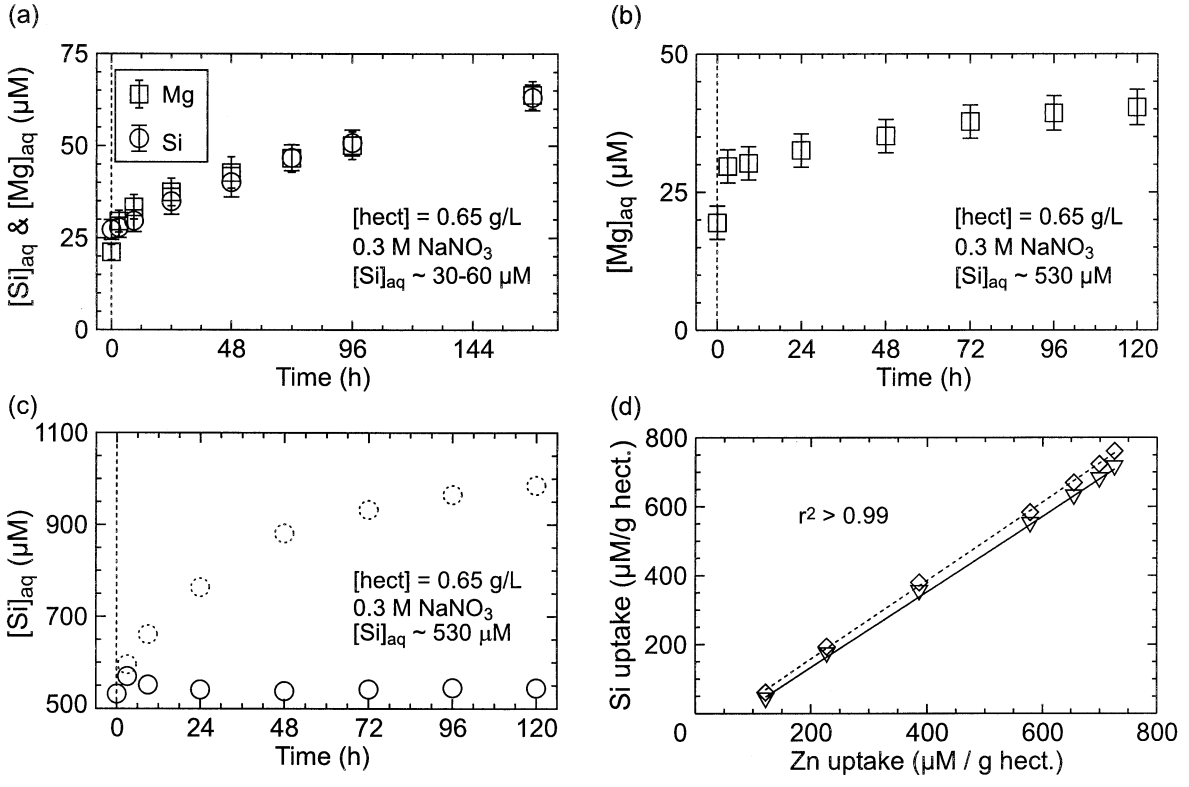

Fig. 3. Impact of Zn uptake on Mg and Si concentrations in the suspension. Error bars represent the uncertainty in analytical measurements. These bars are not shown when smaller than the symbols. (a) $[Mg]_{aq}$ (⊞) and $[Si]_{aq}$ (⊕) in solution for [hect] = 0.65 g L^{-1} and $[Si]_{aq}$ ~30–60 μM, Sample H30_Zn. (b) $[Mg]_{aq}$ (⊞) in solution for [hect] = 0.65 g L^{-1} and $[Si]_{aq}$ ~530 μM. Sample H30_SiZn. (c) $[Si]_{aq}$ (H30_SiZn). (○): Measured concentration. (◌): Calculated concentration assuming that all Si added during Zn sorption remained in the supernatant. (d) Plot of Si uptake vs. Zn uptake for H30_SiZn. (▽): Si uptake calculated from the difference between Si added with silica base solution and Si remaining in solution; regression slope of 1.09 ± 0.08 (solid line). (◇): Si uptake calculated from the difference between Si added with silica base solution plus Si released by congruent dissolution of hectorite and Si remaining in solution; regression slope of 1.14 ± 0.09 (dashed line).

Mesmer, 1976). Calculation of saturation indices Ω (defined as the ratio of the ion activity product, IAP, to the solubility constant K_{eq}; Stumm and Morgan, 1996), using the Davies equation for activity coefficients and assuming uncertainties on these coefficients as high as 0.2, showed that $[Zn]_{aq}$ never reached the solubility limits of ZnO ($\Omega_{ZnO} = (Zn^{2+})/[(H^+)^2.K_{eq}^{ZnO}] = 0.4 \pm 0.3$ at t = 0, where (Zn^{2+}) and (H^+) are the activities of Zn^{2+} and H^+ in solution) and $Zn(OH)_2$ ($\Omega_{Zn(OH)2} = (Zn^{2+})/[(H^+)^2.K_{eq}^{Zn(OH)2}] = 0.1 \pm 0.08$ at t = 0; Baes and Mesmer, 1976). Complexation of Zn by dissolved Si was not considered because to our knowledge no thermodynamic data are available.

2.3. Sample Preparation for EXAFS Spectroscopy

Fifteen microns thick self-supporting films of Zn-sorbed hectorite were obtained by slowly filtering on 0.05 μm Sartorius cellulose nitrate filters 40 mL of reacted suspensions withdrawn at t = 9 h, 120 h (H30_SiZn), and 96 h (H30_Zn). Filtration was performed in a closed vessel under a continuous flow of humidified Ar to limit contamination by atmospheric carbonate. Excess salt and aqueous Zn in the wet films were removed with a few milliliters of deionized water before drying. Previous experiments showed that drying does not modify the molecular environment of Zn sorbed at high ionic strength (Schlegel et al., 2001). Seven to eight slices of the same film were cut and stacked on a sample holder. On stacking, the slices were successively rotated around an axis perpendicular to the film plane to improve, if possible, the in-plane disorientation of hectorite crystallites. A fraction of NoH_SiZn at t = 125 h (NoH_SiZn_125h) was pipetted into a Teflon sample holder sealed with kapton windows for fluorescence-yield EXAFS measurements. Sample names and chemical conditions for the preparation of EXAFS samples are summarized in Table 1.

2.4. EXAFS Data Collection and Reduction

Zn K-edge EXAFS spectra were recorded at the European Synchrotron Radiation Facility (ESRF, France) on the BM32 CRG/IF station. The optics of the spectrometer consists of a Ni-coated focusing mirror and an Si(111) double-crystal monochromator equipped with a sagittal focusing (Hazemann et al., 1995). Clay films were mounted on a goniometer, and EXAFS spectra were recorded at α = 10°, 35°, 55°, and 80°. The most concentrated sample (H30_SiZn_120h) was recorded in transmission mode, using photodiode detectors. The three other samples (H30_SiZn_9h, H30_Zn_96h, and NoH_SiZn_125h) were recorded in fluorescence detection mode, using a 30-element array Ge detector. The EXAFS spectrum of NoH_SiZn_125h was recorded immediately after its transfer into the Teflon cell.

EXAFS data were reduced with the SEDEM software (Aberdam, 1998). As a preliminary step, absorption spectra were given the shape of the Stobbe function, which is a quantum-mechanically derived formula for atomic absorption. Fourier transformations were performed on $k^3\chi(k)$ functions between k = 2.5 and 12 $Å^{-1}$ using a Kaiser apodization window (Manceau and Combes, 1988). Fourier transforms (FTs) display amplitude maxima (peaks) located at apparent absorber-backscatterer distances (R + ΔR), which differ from interatomic structural distances (R) by $\Delta R \sim -0.3$ to -0.4 Å (Teo, 1986). FT peaks of interest were selected in distance space and Fourier back-transformed in k space by using a software package written by D. Bonnin (ESPCI, Paris). R-values and numbers of atomic neighbors (N^α) were determined by least-squares fitting of Fourier-filtered EXAFS contributions [χ^{exp} (k)] with theoretical phase and amplitude functions calculated using FEFF7.02 (Rehr et al., 1992). Zn talc and Zn-doped talc were used as model structures for Zn-O, Zn-Zn, Zn-Mg, and Zn-Si pairs (Rayner and Brown, 1973). The amplitude reduction factor S_0^2 was set to 0.85 (O'Day et al., 1994b; Manceau et al., 1998). Goodness of fit was quantified by the reliability factor R_P, defined as

$$R_p = \frac{\sum_k (k^3 \cdot \chi^{calc}(k) - k^3 \cdot \chi^{exp}(k))^2}{\sum_k (k^3 \cdot \chi^{exp}(k))^2} \quad (2)$$

where χ^{calc} (k) is the calculated EXAFS contribution. The precision on EXAFS distances (R^{EXAFS}) was previously estimated to be $\pm$ 0.02 Å for $R_{Zn\text{-}O}^{EXAFS}$ and $\pm$ 0.03 Å for $R_{Zn\text{-}Zn}^{EXAFS}$, $R_{Zn\text{-}Mg}^{EXAFS}$, and $R_{Zn\text{-}Si}^{EXAFS}$ (Schlegel et al., 2001). The accuracy (absolute precision) and uncertainty (relative precision) on N^α is discussed below. Multiple scattering contributions to the second FT peak were not considered in the fitting procedure, as they were shown to be extremely weak (Manceau et al., 1998).

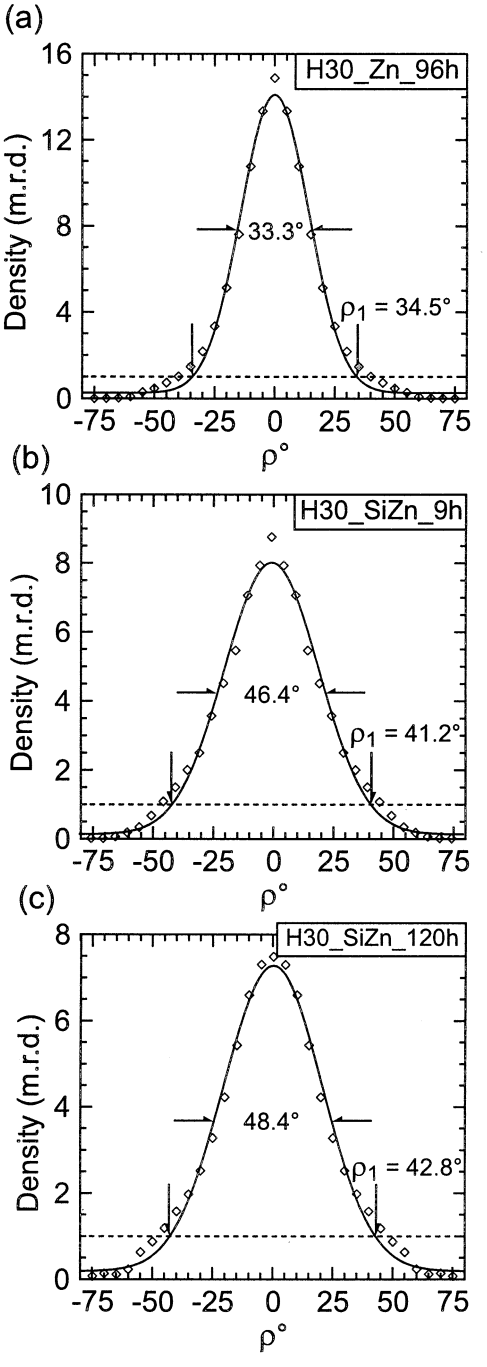

Fig. 4. Integrated radial distribution densities of *c** axes of hectorite crystallites with respect to the normal of the self-supporting film (ρ = 0°). The 1-m.r.d. level (perfectly random powder) is indicated by a dashed line. Linear density scales and equal area projections are used for the pole figures. (a) H30_Zn_96h. (b) H30_SiZn_9h. (c) H30_SiZn_120h. Note the decrease in texture strength from H30_Zn_96h to H30_SiZn_120h, presumably resulting from a modification of the textural properties of the clay platelets.

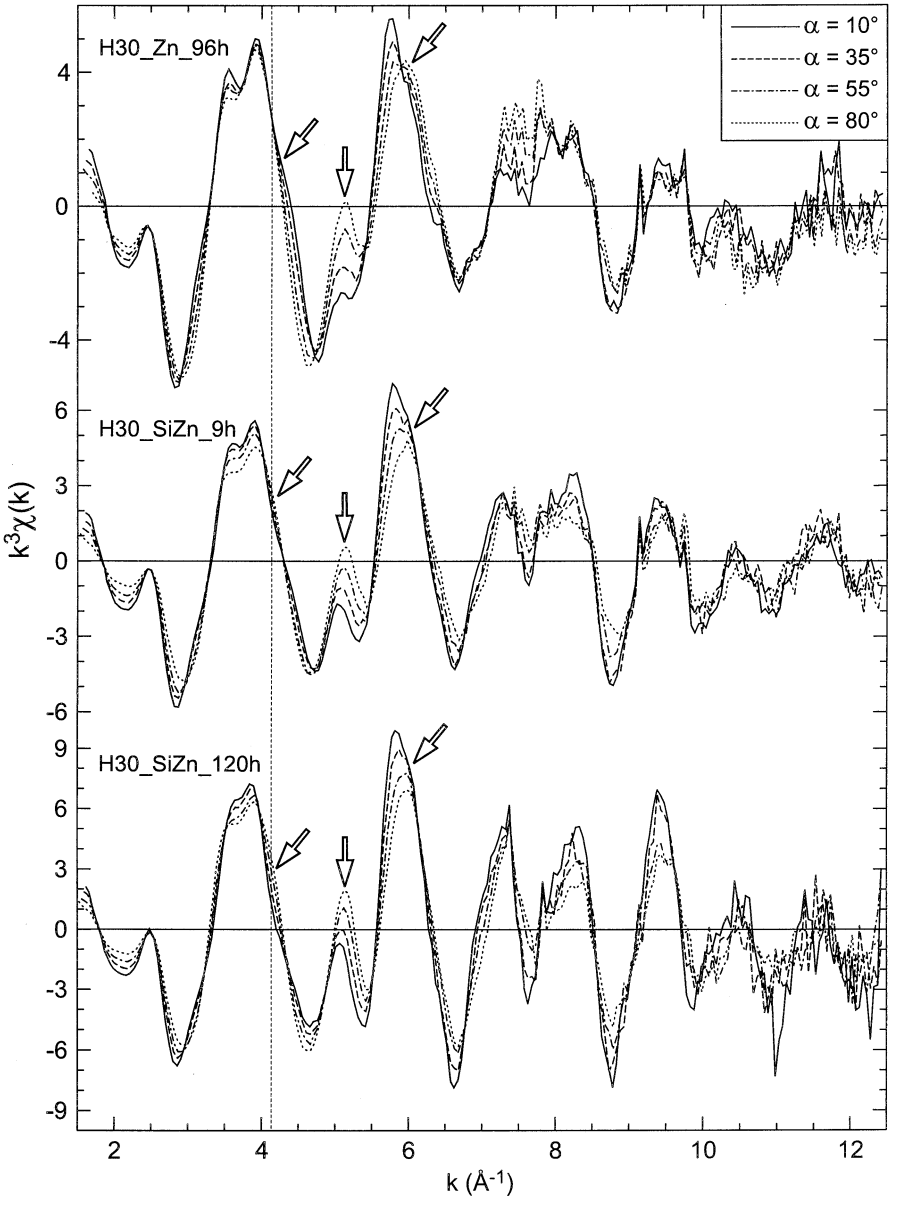

Fig. 5. k^3-weighted Zn K-edge P-EXAFS spectra for Zn-sorbed hectorite films at α angles of 10, 35, 55, and 80°. Chemical conditions for samples are listed in Table 1.

2.5. Quantitative Texture Analysis

Orientation distributions of the c^* axes of the hectorite particles within the self-supporting films were determined by texture goniometry on single film slices, using a four-circle HUBER Cradle diffractometer. The incident beam (Cu Kα) was monochromatized and collimated on the sample (1 × 1 mm slits), with a divergence of 7 × 7 mrad in the asymmetric reflection mode. The {004} pole figures were obtained by tilting the angle between the normal to the film and the plane containing the incident and diffracted X-ray beams (ρ) by $\Delta\rho = 5°$ increments over the [−80°, 80°] ρ-range, and recording the diffraction pattern for each ρ step over a θ Bragg interval of 120° with a position-sensitive curved detector (INEL CPS 120; counting time: 1800 s per step). Since self-supporting films of fine-grained layer minerals have an axisymmetrical fiber-like texture (i.e., random in-plane distribution of crystallite a and b axes), the distribution density of c^* axes off the film normal is simply retrieved from the integrated intensity I(ρ) of the {004} reflection as a function of ρ after background subtraction (Manceau et al., 2000).

3. RESULTS

3.1. Kinetics

No change in $[Zn]_{aq}$ was observed in experiment NoH_SiZn, even after 125 h of reaction time (Fig. 2). Since this sample was prepared without hectorite, this result indicates that Zn precipitates did not nucleate in solution or that such nuclei were too small to be removed by centrifugation and filtration. On the other hand, Zn uptake was observed in H30_SiZn and H30_Zn,

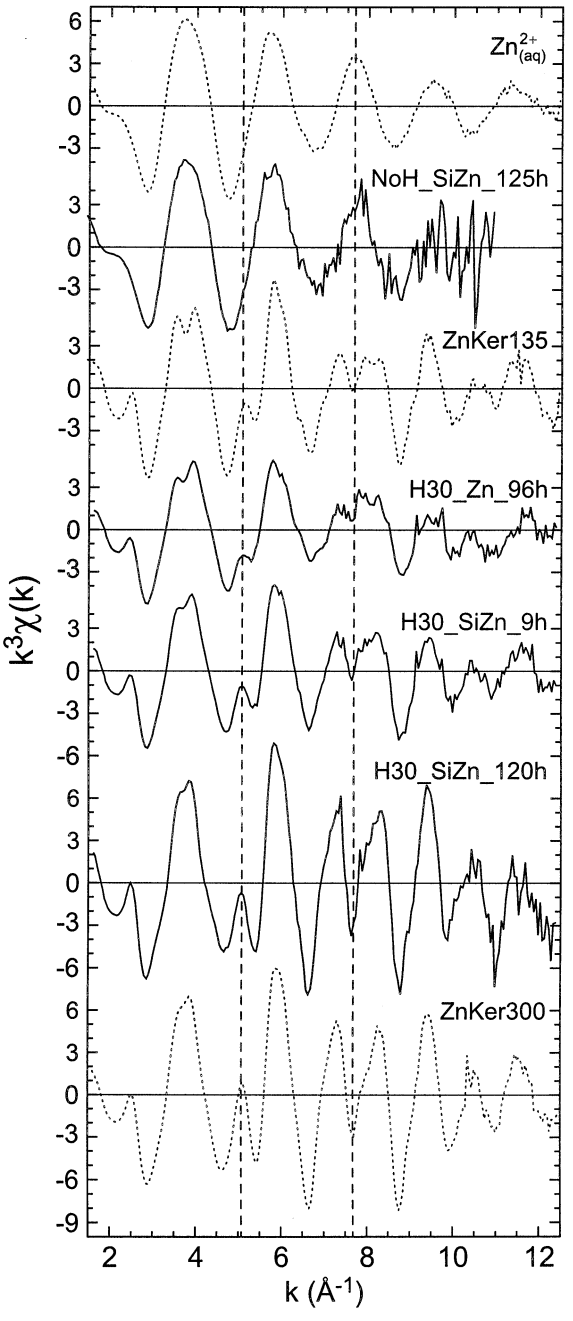

Fig. 6. k^3-weighted Zn K-edge EXAFS spectra for aqueous Zn ($Zn^{2+}_{(aq)}$) Zn-rich kerolite (ZnKer135, ZnKer300) references, and for Zn-sorbed hectorite films. All spectra were recorded at the magic angle ($\alpha = 35°$).

indicating that Zn was sorbed by hectorite. Distinct kinetics of Zn uptake was observed for H30_SiZn and H30_Zn. When no Si was added (H30_Zn), 5.8% of TotZn (46.6 μmol g^{-1} hectorite) was sorbed during the first 3 h of reaction time. Afterwards, Zn sorption slowed (from 4.3 ± 0.3 to 0.10 ± 0.03 nmol s^{-1} g^{-1} hectorite) and only 14.6% of TotZn (117 μmol g^{-1} hectorite) was sorbed at t = 168 h. Initial Zn sorption was more rapid for H30_SiZn (11.3 ± 0.3 nmol s^{-1} g^{-1} hectorite at t = 3 h), and sorbed Zn amounted to 15.2% of TotZn (122 μmol g^{-1} hectorite) at t = 3 h. Furthermore, Zn sorption continued, and 90.7% of TotZn (725 μmol g^{-1} hectorite) was sorbed at t = 120 h. The influence of Zn uptake on hectorite dissolution and on fluctuations of $[Si]_{aq}$ was also examined. In the absence of hectorite (NoH_SiZn), $[Si]_{aq}$ and $[Mg]_{aq}$ remained constant ($[Si]_{aq}$ = 530 μM and $[Mg]_{aq}$ = 30 μM). In the low $[Si]_{aq}$ experiment (H30_Zn), $[Si]_{aq}$ and $[Mg]_{aq}$ steadily increased with time, indicating that hectorite dissolved during Zn uptake (Fig. 3a). The ratio of Si to Mg release [(36 ± 7)/(43 ± 7) = 0.84 ± 0.21] is less than the Si : Mg stoichiometric ratio in hectorite (1.49), suggesting incongruent dissolution. This incongruency can result either from excess Mg release or from back uptake of dissolved Si. An increase of $[Mg]_{aq}$ with reaction time was also observed for H30_SiZn, supporting dissolution of hectorite even at "high" $[Si]_{aq}$ (Fig. 3b). In contrast, $[Si]_{aq}$ values at the beginning and end of H30_SiZn were comparable (solid circles in Fig. 3c), even though large volumes of basic silica solution were added during the entire reaction time to keep the pH at 7.30. To clarify, let us assume that all Si added with basic silica had accumulated in the supernatant. Theoretical $[Si]_{aq}$ as a function of time can be calculated from the increments of added basic silica, taking the measured $[Si]_{aq}$ at t = 0 as a starting value. Comparing experimental and calculated $[Si]_{aq}$ (solid vs. dotted circles in Fig. 3c) shows that Si uptake occurred during Zn uptake. The correlation between calculated Si and experimental Zn uptakes for t ≥ 3 h is linear (Fig. 3d) with 1.09 (± 0.08) mols of Si sorbed per mol of sorbed Zn, suggesting that the same molecular mechanism may be responsible for uptake of both elements. However, the experimental Si/Zn uptake ratio is lower than Si/Zn = 1.33 for a TOT [$Zn_3Si_4O_{10}(OH)_2$], and higher than Si/Zn = 0.67 for a TO [$Zn_3Si_2O_5(OH)_4$] phyllosilicate. This calculation does not take into account uptake of Si that may be supplied by dissolution of hectorite. This supply, calculated from $[Mg]_{aq}$ assuming stoichiometric dissolution, leads to Si/Zn = 1.14 ± 0.09, which still does not match either TO or TOT ratios. Further insight on the molecular mechanism of Zn and Si sorption was obtained by P-EXAFS spectroscopy.

3.2. Quantitative Texture Analysis

The distribution density of crystallite c^* axes off the film normal is visualized by the radial distribution density of {004} poles (Fig. 4). In a random isotropic powder, crystallites are distributed over all possible orientations and consequently, $I(\rho)$ is constant after correcting the X-ray defocusing. Here, narrow distributions with maxima near $\rho = 0°$ are observed, which indicates that most platelets have their c^* axes normal to the film plane (i.e., *ab* planes are parallel to the film plane). H30_Zn_96h was highly textured, with a measured maximum of distribution density (P_{max}, expressed as multiple of random distribution or m.r.d.), equal to 14 m.r.d. and a full width at half-maximum (FWHM) of the distribution equal to 33.3°. c^* axes have larger angular spread in H30_SiZn_9h (P_{max} = 8.7 m.r.d., FWHM = 46.4°) and H30_SiZn_120h (P_{max} = 7.5 m.r.d., FWHM = 48.4°). The decrease in orientation strength parallels the increase in Zn content (Table 1) and suggests a modification of the surface properties of clay particles in the films as a result of Zn sorption. Manceau and Schlegel (2001) showed that no significant attenuation of the

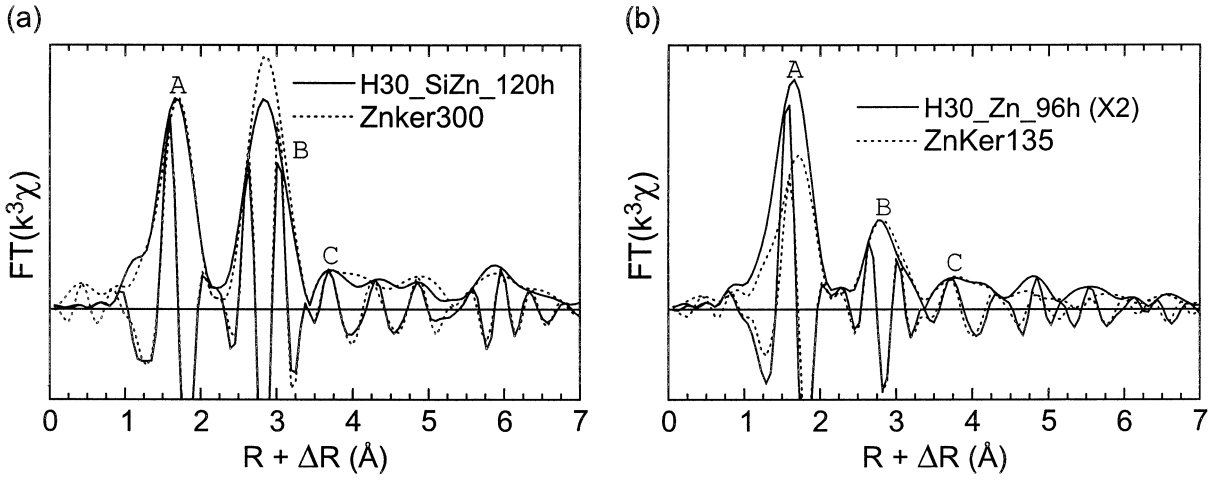

Fig. 7. Comparison of k^3-weighted Fourier transforms (moduli and imaginary parts) for (a) H30_SiZn_120h at $\alpha = 35°$ and ZnKer300, (b) H30_Zn_96h at $\alpha = 35°$ and ZnKer135.

angular dependence of P-EXAFS spectra occurs when the FWHM of the angular spread is < 40 to 50° for parallel measurement, and < 30 to 40° for normal measurement. Therefore, the higher disorientation in the two most concentrated samples diminishes, but does not suppress, polarization dependence of P-EXAFS spectra.

3.3. EXAFS Spectroscopy

3.3.1. EXAFS spectra

k^3-weighted P-EXAFS spectra for sorption samples show the presence of multiple frequencies with high amplitudes at high k (e.g., k = 8 $Å^{-1}$), indicating the existence of several structurally ordered atomic shells around Zn (Fig. 5). The strong polarization dependence of the amplitude and position of EXAFS oscillations, e.g., near 5.2 and 6.0 $Å^{-1}$, indicates that Zn atoms are structurally linked to hectorite platelets. However, the three EXAFS spectra have distinct spectral features (e.g., near k = 4.1 $Å^{-1}$), angular dependencies (see arrows in Fig. 5), and even amplitudes. These dissimilarities point to a diversity of Zn crystallochemical environments. Spectral modifications between samples are also shown in Figure 6, which compares EXAFS spectra for sorption samples at $\alpha = 35°$ (at this angle, P-EXAFS spectra and powder EXAFS spectra are similar; Manceau et al., 1990) to structural references. These references include a Zn kerolite, $Zn_3Si_4O_{10}(OH)_2$ (ZnKer300), and a mixed (Zn, Mg)-kerolite, $Zn_{1.35}Mg_{1.65}Si_4O_{10}(OH)_2$ (ZnKer135). Both compounds have a structure like hectorite in which Zn is located in the octahedral sheet and is surrounded by four out-of-plane Si neighbors of the tetrahedral sheets at R ≈ 3.25 Å, and either 6 Zn (ZnKer300) or 2.7 Zn + 3.3 Mg (ZnKer135) in-plane cations of the octahedral sheet at R ≈ 3.10 Å (Decarreau, 1985; Schlegel et al., 2001). ZnKer135 and H30_Zn_96h have a similar shape, indicating that Zn in the clay film is located in a phyllosilicate environment with both Mg and Zn octahedral neighbors as in ZnKer135 (Fig. 6). Likewise, the spectral resemblance between ZnKer300 and H30_SiZn_120h is notable, and suggests that the crystallochemical environments of Zn in the two solids are alike.

The EXAFS spectrum for NoH_SiZn_125h is quite different from those of the films and displays a single-wave frequency like the solvated $Zn^{2+}_{(aq)}$ reference. This result shows that homogenous nucleation of Zn solid phases in bulk solution is a marginal process if it occurs at all and proves that Zn reacted directly with hectorite surfaces in the sorption samples.

3.3.2. Fourier transforms (FTs)

Insight on the crystallochemical environment of Zn can be obtained by comparing moduli (|FT|s) and imaginary parts of Fourier transforms for sorption samples and kerolite references (Fig. 7a,b). The imaginary parts and positions of |FT|s maxima for H30_SiZn_120h and ZnKer300 coincide over the entire R + ΔR range (Fig. 7a). This similarity confirms that Zn in the sorption sample is located in the octahedral sheet of a phyllosilicate structure and surrounded by in-plane Zn neighbors at R ~3.10 Å and out-of-plane Si neighbors at R ~3.25 Å, as in ZnKer300 (Manceau et al., 1999a). The FT for H30_Zn_96h resembles ZnKer135, differing only in amplitude at low and high R + ΔR values (Fig. 7b). Again, this similarity provides strong evidence for the location of sorbed Zn in a clay-like environment with Zn being surrounded by Zn, Mg, and Si as in ZnKer135. These spectral similarities simplify the structural assignment of FT peaks observed at R + ΔR = 1.7 Å (peak A; Fig. 8), 2.7 to 2.8 Å (peak B), and 3.8 Å (peak C) for the sorption samples as described below.

Peak A originates from the contribution of oxygen atoms ligated to Zn (Manceau et al., 2000). $R^{EXAFS}_{Zn\text{-}O}$ values obtained by least-squares fitting of Fourier-filtered χ^{α}_{O} functions equal 2.04 Å for H30_Zn_96h (σ = 0.10 Å), 2.05 Å for H30_SiZn_9h (σ = 0.10 Å) and 2.06 Å for H30_SiZn_120h (σ = 0.09 Å; Table 2). The variations in distances are within uncertainty. These values are typical of sixfold coordinated Zn, as fourfold coordination yields $R^{EXAFS}_{Zn\text{-}O} < 2$ Å (Kuzmin et al., 1997; Sarret et al., 1998). The decrease of σ correlates with an

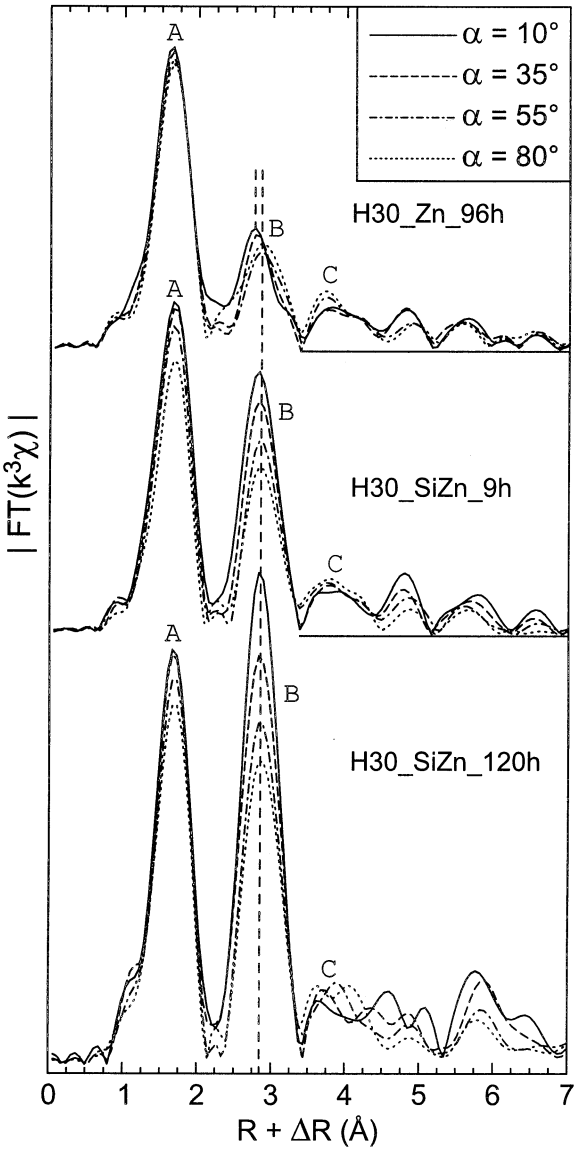

Fig. 8. Moduli of the Fourier transforms (|FT|s) for Zn-sorbed hectorite films at α angles of 10, 35, 55, and 80°. Chemical conditions for samples are listed in Table 1.

increase of N_O^α at given α (Table 2), and the evolution of these structural parameters accounts for the experimental increase in amplitude of peak A from H30_Zn_96h, to H30_SiZn_9h, and to H30_SiZn_120h (Fig. 8). This trend can be related to an increase in structural order of Zn coordination octahedra, i.e., a narrower dispersion of Zn-O bond lengths. The relatively high spread of Zn-O bond lengths for H30_Zn_96h probably results from Zn coordination to oxygens of distinct chemical entities with contrasted bonding strengths, such as H_2O molecules, OH groups, and possibly oxygen atoms of the sorbent surface (Schlegel et al., 1999a). Alternatively, the higher structural order observed for H30_SiZn_120h is consistent with the formation of a clay mineral, in which octahedral Zn is coordinated to only OH groups and O atoms as in phyllosilicates. Also, from H30_Zn_96h, to H30_SiZn_9h, and to H30_SiZn_120h, the number of neighboring O at $\alpha = 35°$ (at this angle the number of backscatterers detected in polarized and powder spectra are the same) becomes closer to $N_O^{35°} = 6$ expected from $R_{Zn\text{-}O}^{EXAFS}$ distances. This trend indicates an increasing accuracy in $N_O^{35°}$ measurements with increasingly ordered backscattering oxygen shells.

How the comparison of experimental N_O^α values on independent EXAFS spectra recorded at successive α angles allows us to estimate the uncertainty of these values is shown here. The apparent number of neighbor atoms in a given j shell is (Schlegel et al., 1999a):

$$N_j^\alpha = N_j^{35°} \cdot \left[\frac{3}{2}(1 - 3\cos^2\beta_j)\cos^2\alpha + 3\cos^2\beta_j\right], \qquad (3)$$

where $N_j^{35°}$ is the number of backscatterers in a powder sample, and β is the inclination angle of the j shell with respect to c^*. Because Eqn. 3 requires that N_j^α be a linear function of $\cos^2\alpha$, any deviation from this linearity can in turn be used to estimate the uncertainty on N_j^α when α is varied. This uncertainty σ_N can be simply retrieved from (Taylor, 1997):

$$\sigma_N = \frac{t_{95,2}}{\sqrt{n}} \cdot \sqrt{\frac{\sum_\alpha (N_j^\alpha - \overline{N_j^\alpha})^2}{n - 2}}, \qquad (4)$$

where n is the number of data points (here $n = 4$), $t_{95.5,2} = 4.303$ is the student t parameter at a 95% confidence level with two degrees of freedom, and $\overline{N_j^\alpha}$ is the number of neighbor atom recalculated from the linear regression of experimental N_j^α with respect to $\cos^2\alpha$. Results in Table 2 show that angular variations of N_O^α values for each sample are within uncertainty, suggesting that the inclination angle β_O is probably close to 54.7°.

Peak B results from the contribution of neighboring cations from the octahedral (Oct) and tetrahedral (Tet) sheets (Manceau et al., 2000). Its amplitude, position, and angular dependence depend on the phase relation between the EXAFS contributions from Zn-Oct and Zn-Tet pairs. For instance, the invariance in phase and position of peak B with α for H30_SiZn_120h (Fig. 9a) indicate that the χ_{Oct} and χ_{Tet} waves are in phase, as typically observed when the X-ray absorber atom is surrounded by "heavy" atoms (e.g., Fe, Co, Ni, Zn) in the Oct sheet and "light" atoms (e.g., Si, Al) in Tet sheets (Manceau et al., 1998). Based on the chemical composition of the present sorbent-sorbate system, the heavy atoms undoubtedly correspond to Zn and the light atoms to Si. In contrast, peak B in H30_Zn_96h displays a complex polarization dependence: Its amplitude decreases from $\alpha = 10°$ to $\alpha = 55°$ and then increases as α converges to 80° and its position and imaginary parts shift with α (Fig. 9b). In trioctahedral smectites, this angular behavior is characteristic of in-plane Mg and out-of-plane Si contributions (Schlegel et al., 1999a). However, FT similarity between H30_Zn_96h and ZnKer135 (Fig. 9b) indicates that an additional in-plane contribution from Zn backscatterers cannot be precluded. Finally, an intermediate angular dependence is observed for H30_SiZn_9h, suggesting that the Zn environment in this last sample is comprised between H30_Zn_96h and H30_SiZn_120h.

Optimal fit of the Fourier-filtered $\chi_B^{80°}$ (k) function for

Table 2. Quantitative EXAFS analysis of the Zn-O coordination shell.

Samples	α	IFT range[a] (Å)	R (Å)	N_O^α	σ_N[b]	σ (Å)	ΔE_0[c] (eV)	N_{fit}[d]	R_P
H30_Zn_96h	10°	1.1–2.2	2.04[e]	4.5	0.2	0.10[d]	−1.4[e]	1	0.010
	35°	1.0–2.2	2.04	4.4	0.2	0.10	−1.4	4	0.006
	55°	1.0–2.2	2.04[e]	4.3	0.2	0.10[d]	−1.4[e]	1	0.007
	80°	1.1–2.2	2.04[e]	4.4	0.2	0.10[d]	−1.4[e]	1	0.002
H30_SiZn_9h	10°	1.1–2.2	2.05[e]	5.1	0.4	0.10[d]	−1.5[e]	1	0.002
	35°	1.1–2.2	2.05	5.0	0.4	0.10	−1.5	4	0.002
	55°	1.1–2.2	2.05[e]	4.8	0.4	0.10[d]	−1.5[e]	1	0.001
	80°	1.1–2.1	2.05[e]	4.2	0.4	0.10[d]	−1.5[e]	1	0.004
H30_SiZn_120h	10°	1.2–2.2	2.06[e]	6.1	0.3	0.09[d]	−1.4[e]	1	0.007
	35°	1.2–2.2	2.06	6.0	0.3	0.09	−1.4	4	0.010
	55°	1.2–2.2	2.06[e]	5.9	0.3	0.09[d]	−1.4[e]	1	0.002
	80°	1.1–2.2	2.06[e]	5.5	0.3	0.09[d]	−1.4[e]	1	0.002

[a] R + ΔR interval for inverse Fourier transform (IFT) in the real space.
[b] Uncertainty on N_o^α at the 95% confidence level.
[c] Threshold energy E_0 taken at the half-height of the absorption edge ($\Delta\mu/2$).
[d] Number of fitting parameters. N_{fit} were always lower than the degree of freedoms of the fit N_{free}, calculated as $N_{free} = (2\delta k\delta R/\pi) + 2$, where δk (Å^{-1}) is the k-space range of the spectral fit and δR (Å) is the R+ΔR space range of the inverse Fourier transform (Stern, 1993).
[e] Value fixed during the fitting procedure.

H30_Zn_96h (R_p = 0.019) was obtained with a Si shell of 3.6 atoms at $R_{Zn\text{-}Si}^{EXAFS}$ = 3.28 Å (σ_{Si} = 0.10 Å; Fig. 10a). In phyllosilicate structures, this shell is not completely extinguished for parallel measurement (Manceau et al., 1998). Attempts to fit $\chi_B^{10°}$ (k) with a combination of either (Mg + Si) or (Zn + Si) atomic shells failed and both Zn and Mg shells had to be included. To reduce the degree of freedom of the fit, the following constrains were applied: $R_{Zn\text{-}Mg}^{EXAFS} = R_{Zn\text{-}Zn}^{EXAFS}$, $\sigma_{Mg} = \sigma_{Zn}$, and $R_{Zn\text{-}Si}^{EXAFS}$ and σ_{Si} were fixed to their values at α = 80°. The number of fitting parameters was therefore lower than the degree of freedom of the fits (Table 3). A good fit (R_p = 0.025) was obtained with $R_{Zn\text{-}Zn,\ Mg}^{EXAFS}$ = 3.08 Å, $N_{Zn}^{10°}$ = 1.9, $N_{Mg}^{10°}$ = 1.9, and $N_{Si}^{10°}$ = 0.4 ($\sigma_{Zn,\ Mg}$ = 0.10 Å; Table 3). χ_B^α (k) functions at α = 35° and 55° were then fitted by varying only N_{Zn}^α, N_{Mg}^α, and N_{Si}^α (Table 3).

$\chi_B^{80°}$ (k) for H30_SiZn_120h could not be fitted with a single Si shell. Figure 10 shows that the maximum of $\chi_B^{80°}$ (k) shifts from ~5 Å^{-1} for H30_Zn_96h to ~6 Å^{-1} for H30_SiZn_120h. This suggests that the Zn contribution, which is predominant at α = 10°, is not completely extinguished at α = 80° owing to the imperfect film texture. Therefore, $\chi_B^{10°}$ (k) and $\chi_B^{80°}$ (k) were fitted with a combination of Zn and Si shells by constraining $R_{Zn\text{-}Zn}^{EXAFS}$, $R_{Zn\text{-}Si}^{EXAFS}$, σ_{Zn} and σ_{Si} values to be identical at α = 10 and 80° to decrease the degree of freedom of the fit. Good fits (R_p = 0.004 at α = 10° and 0.008 at α = 80°) were obtained with $R_{Zn\text{-}Zn}^{EXAFS}$ = 3.10 Å, $R_{Zn\text{-}Si}^{EXAFS}$ = 3.26 Å, $N_{Zn}^{10°}$ = 8.0, $N_{Si}^{10°}$ = 2.2, $N_{Zn}^{80°}$ = 2.7, and $N_{Si}^{80°}$ = 6.4 (σ_{Zn} = σ_{Si} = 0.10 Å; Fig. 10c and Table 3). $\chi_B^{35°}$ (k) and $\chi_B^{55°}$ (k) functions were then fitted by varying only N_{Zn}^α and N_{Si}^α (Table 3). Adding an Mg contribution ($R_{Zn\text{-}Mg}^{EXAFS} = R_{Zn\text{-}Zn}^{EXAFS}$; $\sigma_{Mg} = \sigma_{Zn}$) did not improve the fit at α = 10° (R_p = 0.004 for $N_{Mg}^{10°}$

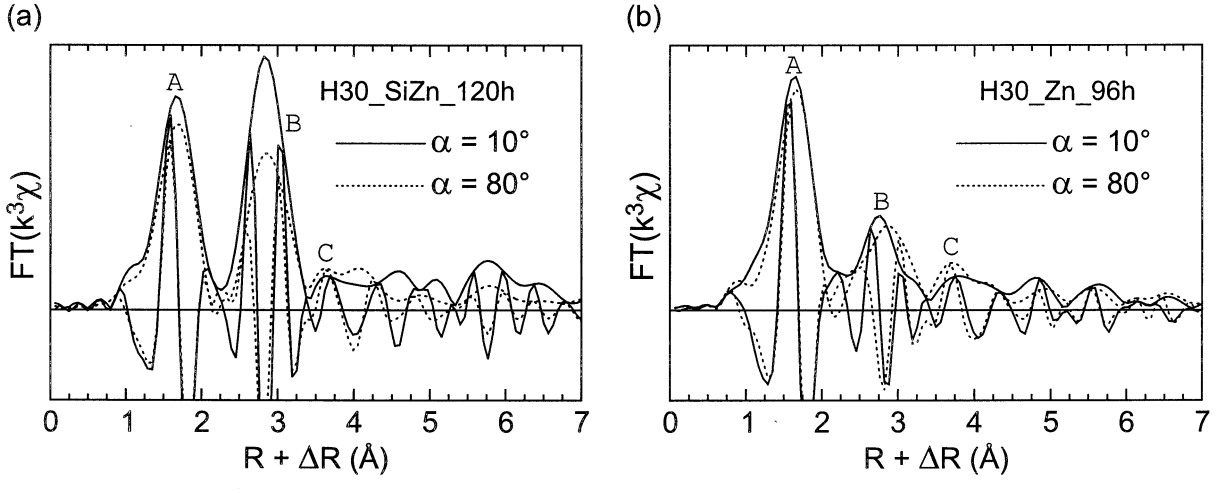

Fig. 9. Comparison of k^3-weighted Fourier transforms (moduli and imaginary parts) for (a) H30_SiZn_120h at α = 10 and 80°, and (b) H30_Zn_96h at α = 10 and 80°.

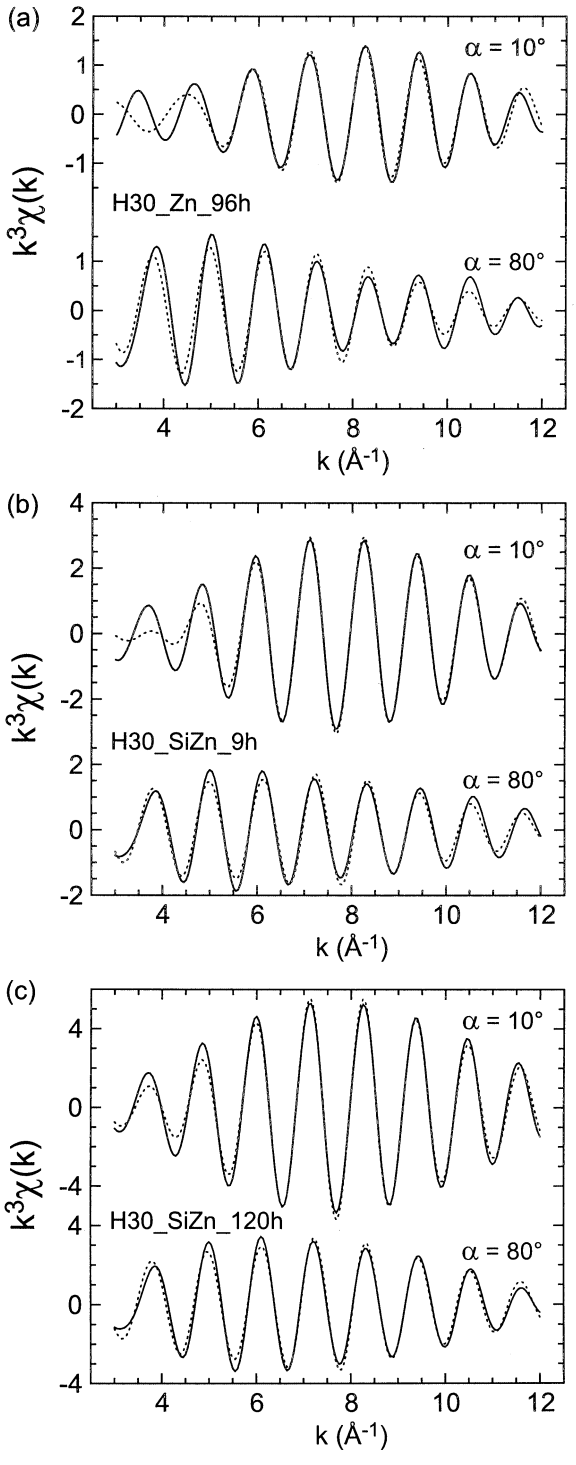

Fig. 10. Fourier-filtered EXAFS contributions of peak B at $\alpha = 80°$ and $\alpha = 10°$ (solid lines) and spectral simulations (dotted lines). (a) H30_Zn_96h. (b) H30_SiZn_9h. (c) H30_SiZn_120h.

= 1) nor at $\alpha = 35°$ ($R_p = 0.011$ for $N_{Mg}^{35°} = 0.5$), which suggests that Mg backscatterers are not significant.

That the shape of the H30_SiZn_9h FT falls between those of H30_Zn_96h and H30_SiZn_120h suggests that Zn, Mg, and Si shells are present in this sorption sample. However, the Mg shell is expected to make only a very weak contribution at $\alpha = 80°$, and therefore it can be safely neglected for the fit of $\chi_B^{80°}$ (k). The $\chi_B^{80°}$ (k) and $\chi_B^{10°}$ (k) functions for H30_SiZn_9h were fitted with Zn and Si contributions at $\alpha = 80°$, and Zn, Mg and Si contributions at $\alpha = 10°$ ($R_{Zn\text{-}Mg}^{EXAFS} = R_{Zn\text{-}Zn}^{EXAFS}$ and $\sigma_{Mg} = \sigma_{Zn}$). To decrease the degree of freedom of the simulation, $R_{Zn\text{-}Zn}^{EXAFS}$, $R_{Zn\text{-}Si}^{EXAFS}$, σ_{Zn}, and σ_{Si} were optimized to identical values at $\alpha = 10$ and 80°. Optimal fits were obtained at $\alpha = 80°$ ($R_p = 0.023$) with 3.8 Si at $R_{Zn\text{-}Si}^{EXAFS} = 3.26$ Å ($\sigma_{Si} = 0.10$ Å) and 1.4 Zn at $R_{Zn\text{-}Zn}^{EXAFS} = 3.10$ Å ($\sigma_{Zn} = 0.10$ Å), and at $\alpha = 10°$, with $N_{Zn}^{10°} = 4.7$, $N_{Mg}^{10°} = 1.1$, and $N_{Si}^{10°} = 0.5$ ($R_P = 0.002$; Fig. 10b and Table 3). The $\chi_B^{35°}$ (k) and $\chi_B^{55°}$ (k) functions were also fitted with Si, Zn, and Mg shells by varying only N_{Zn}^{α}, N_{Mg}^{α}, and N_{Si}^{α} (Table 3). The uncertainty on the measured number of neighboring cations was calculated from Eqn. 4 (Table 3). Note that the presence of an Si shell in H30_Zn_96h is confirmed by this quantitative analysis because $N_{Si}^{\alpha} = 2.8$ and 3.6 for $\alpha \geq 55°$ are significantly above the uncertainty ($\pm$ 1.1).

The $R_{Zn\text{-}Zn}^{EXAFS}$, $R_{Zn\text{-}Mg}^{EXAFS}$, and $R_{Zn\text{-}Si}^{EXAFS}$ values in sorption samples are similar to those in the ZnKer300 and ZnKer003 references (Schlegel et al., 2001) and are characteristic of edge-sharing linkages between Zn and (Zn, Mg) octahedra and of corner-sharing linkages between Zn octahedra and Si tetrahedra as in a phyllosilicate structure. This interpretation is further supported by angular variations of N_j^{α}, because N_{Si}^{α} gradually increases, and N_{Zn}^{α} and N_{Mg}^{α} gradually decrease, with increasing α, implying $\beta_{Si}^{exp} < 54.7°$ (out-of-plane orientation) and $\beta_{Zn,Mg}^{exp} > 54.7°$ (in-plane orientation) as in phyllosilicate structures (Table 3).

Peak C in phyllosilicates was shown to originate from the contribution of next-nearest Si cations (Tet2) at ~4.4 to 4.5 Å and from higher oxygen shells (Manceau et al., 1998). The presence of a Tet2 shell at this distance is characteristic of a layered structure in which Si tetrahedra are polymerized in a two-dimensional framework linked to an octahedral sheet (Fig. 1). Therefore, the occurrence of this peak in all FTs of sorption samples, and the superposition of the FT imaginary parts to those of the clay references (Fig. 7a,b) provide additional support for a clay-like local environment around Zn. The similar amplitude of peaks C in H30_SiZn_120h and in ZnKer300 suggests that Si sheets connected to Zn domains are equally structured in the sorption sample and in the reference. In contrast, the lower amplitude of peak C observed for H30_Zn_96h results either from a greater structural disorder, from smaller tetrahedral sheets, or from a substantial amount of missing Si atoms in these sheets (i.e., incomplete two-dimensional framework).

4. DISCUSSION

4.1. Structure of Zn Complexes and Mechanism of Zn Sorption

In all sorption samples, the existence of in-plane Zn-Zn pairs at 3.08 to 3.10 Å and out-of-plane Zn-Si pairs at 3.26 to 3.28 Å attests for the formation of Zn octahedral sheets parallel to the *ab* plane of hectorite crystallites and bridged to out-of-plane Si tetrahedra. Such Zn polymers were not observed in the absence of hectorite even after 125 h of reaction time, but they did form when the sorbate ions were physically in contact with the

Table 3. Quantitative EXAFS analysis of the FT second peaks.

		IFT range[a]	Zn-Zn shell				Zn-Mg shell				Zn-Si shell				ΔE_0[c]		
Samples	α	(Å)	R (Å)	N	σ_N[b]	σ (Å)	R (Å)	N	σ_N[b]	σ (Å)	R (Å)	N	σ_N[b]	σ (Å)	(eV)	N_{fit}[d]	R_P
H30_Zn_96h	10°	2.3–3.4	3.08[f]	1.9	0.6	0.10[g]	3.08[f]	1.9	0.3	0.10[g]	3.28[e]	0.4	1.1	0.10[e]	−1.4[e]	5	0.025
	35°	2.4–3.4	3.08[e]	1.7	0.6	0.10[e]	3.08[e]	1.4	0.3	0.10[e]	3.28[e]	0.6	1.1	0.10[e]	−1.4[e]	3	0.033
	55°	2.3–3.4	3.08[e]	0.5	0.6	0.10[e]	3.08[e]	0.8	0.3	0.10[e]	3.28[e]	2.8	1.1	0.10[e]	−1.4[e]	3	0.015
	80°	2.2–3.4			0.6				0.3		3.28	3.6	1.1	0.10	−1.4[e]	3	0.019
H30_SiZn_9h	10°	2.1–3.5	3.10[f,h]	4.7	0.2	0.10[g,h]	3.10[f]	1.1	0.2	0.10[g]	3.26[e,h]	0.5	0.4	0.10[e,h]	−1.5[e]	7	0.002
	35°	2.3–3.4	3.10[e]	3.8	0.2	0.10[e]	3.10[e]	0.8	0.2	0.10[e]	3.26[e]	1.5	0.4	0.10[e]	−1.5[e]	3	0.005
	55°	2.4–3.4	3.10[e]	2.6	0.2	0.10[e]	3.10[e]	0.4	0.2	0.10[e]	3.26[e]	2.4	0.4	0.10[e]	−1.5[e]	3	0.016
	80°	2.3–3.4	3.10[h]	1.4	0.2	0.10[h]		0	0.2		3.26[h]	3.8	0.4	0.10[h]	−1.5[e]	6	0.023
H30_SiZn_120h	10°	2.3–3.4	3.10[h]	8.0	0.4	0.10[h]					3.26[h]	2.2	0.4	0.10[h]	−1.4[e]	6	0.004
	35°	2.3–3.4	3.10[e]	6.0	0.4	0.10[e]					3.26[e]	3.6	0.4	0.10[e]	−1.4[e]	2	0.011
	55°	2.3–3.4	3.10[e]	4.2	0.4	0.10[e]					3.26[e]	4.8	0.4	0.10[e]	−1.4[e]	2	0.006
	80°	2.3–3.4	3.10[h]	2.7	0.4	0.10[h]					3.26[h]	6.4	0.4	0.10[h]	−1.4[e]	6	0.008

[a] R + ΔR interval for inverse Fourier transform (IFT) in the real space.
[b] Uncertainty on N at the 95% confidence level.
[c] Threshold energy E_0 taken at the half-height of the absorption edge ($\Delta\mu/2$).
[d] Number of fitting parameters. For all samples $N_{fit} < N_{free}$, where N_{free} is the degree of freedoms of the fit (Stern, 1993).
[e] Value fixed during the fitting procedure.
[f] Distance parameters coupled at the same value for Zn-Zn and Zn-Mg shells.
[g] σ parameters coupled at the same value for Zn-Zn and Zn-Mg shells.
[h] Parameters optimized simultaneously at α = 10° and 80°.

sorbent. Insight on the structural relationship between Zn polymers and the hectorite surface is obtained from the presence of in-plane Mg neighbors at low Zn content. If these Mg cations were solute species incorporated into Zn polymers, then the proportion of Mg in the (Zn, Mg) sheets, and thus $N_{Mg}^{35°}/N_{Zn}^{35°}$, would have increased with increasing $[Mg]_{aq}/[Zn]_{aq}$ ratio. This increase is not observed for H30_SiZn, as $N_{Mg}^{35°}/N_{Zn}^{35°} = 0.21 \pm 0.08$ at t = 9 h and only 0 ± 0.08 at t = 120 h. Therefore, EXAFS-detected Mg cations must correspond to atoms exposed at the edges of hectorite crystallites, leading to the conclusion that Zn sheets formed in structural continuity with hectorite (Mg, Li) octahedral sheets. These Zn polymers can incorporate Si to form clay minerals as shown below.

Zn domains at the hectorite surface can count various numbers of Zn atoms (Q_{Zn}) leading to different average numbers of Zn-Zn pairs (N_{Zn}; Fig. 11). As EXAFS spectroscopy averages the contribution of Zn atoms located in distinct environments, only the average size of Zn domains can be obtained from EXAFS data, and the distribution of polymer size cannot be determined (Fig. 11; Manceau and Calas, 1986). For example, $N_{Zn}^{35°} = 1.7$ for H30_Zn_96h (Table 3) can be obtained by assuming a mixture of either 30% Zn dimers ($N_{Zn} = 1$) and 70% trimers ($N_{Zn} = 2$), or 28% large octahedral sheets ($N_{Zn} \approx 6$) and 78% monomers ($N_{Zn} = 0$). Likewise, $N_{Zn}^{35°} = 3.8$ for H30_SiZn_9h can be obtained by assuming either Zn polymers of 10 to 20 atoms, or 33% monomers and 67% large octahedral sheets ($Q_{Zn} \geq 200$). Hence, the occurrence of small-size surface complexes cannot be ruled out for both H30_Zn_96h and H30_SiZn_9h. In contrast, $N_{Zn}^{35°} = 6.0 \pm 0.4$ for H30_SiZn_120h indicates that almost all Zn formed relatively large octahedral sheets with $Q_{Zn} \geq 200$, hence, with diameters $\geq$ 30 Å.

4.1.1. Zn sorption at low concentration of dissolved Si

The amount of Zn adsorbed (46 μmol g^{-1}) at pH 7.30 after 3 h of reaction time at low $[Si]_{aq}$ (~30 to 60 μM), and the concomitant rapid release of Mg in the suspension, resemble sorption results at pH 6.50, where sorbed Zn was shown to form mononuclear surface complexes at the layer edges of hectorite (Schlegel et al., 2001). At t = 96 h (H30_Zn_96h), the amount of sorbed Zn reached 91 μmol g^{-1} hectorite, and Zn formed polymers of small mean size (Q_{Zn} = 2–3) bridged to surface Mg octahedra and Si tetrahedra exposed at the edges of sorbent layers (Fig. 12a). As explained above, the occurrence of Zn monomers together with large Zn domains cannot be dismissed, but such large domains would amount to < 20% of sorbed Zn. Hence, Zn is predominantly in oligomeric form. Incorporation of dissolved Si to Zn polymers to neoform hydrous silicate nuclei may partly account for the slight incongruency of hectorite dissolution, yet this incongruency can also be explained by an excess release of Mg upon Zn adsorption (Schlegel et al., 2001). In conclusion, Zn uptake at low $[Si]_{aq}$ and for the investigated sorption time (t < 96 h) results in the formation of small surface oligomers in structural continuity with hectorite octahedral sheets.

4.1.2. Zn sorption at high concentration of dissolved Si

At t = 9 h and $[Si]_{aq}$ ~530 μM (H30_SiZn_9h), the amount of sorbed Zn (227 μmol g^{-1}), the mean size of Zn polymers (Q_{Zn} ~10–20), and the number of neighboring Si atoms ($N_{Si}^{35°}$ = 1.5) were higher than at t = 96 h and $[Si]_{aq}$ ~30–60 μM (H30_Zn_96h). $N_{Si}^{35°} = 1.5$ in H30_SiZn_9h may be accounted for by assuming ~27% of monomeric Zn surface complexes (61 μmol g^{-1}) bound to four Si tetrahedra of the sorbent surface ($N_{Si}^{35°} = 0.27*4 = 1.1 \approx 1.5 \pm 0.4$), and ~73% of large Si-free Zn layers. However, these edge-bridged Zn monomeric complexes should also form at lower $[Si]_{aq}$, yet the low $N_{Si}^{35°}$ value in H30_Zn_96h indicates that they do not, allowing us to discard their formation at higher $[Si]_{aq}$ (Table 3). Alternatively, assuming that Si polymerized with Zn to form Zn clay nuclei

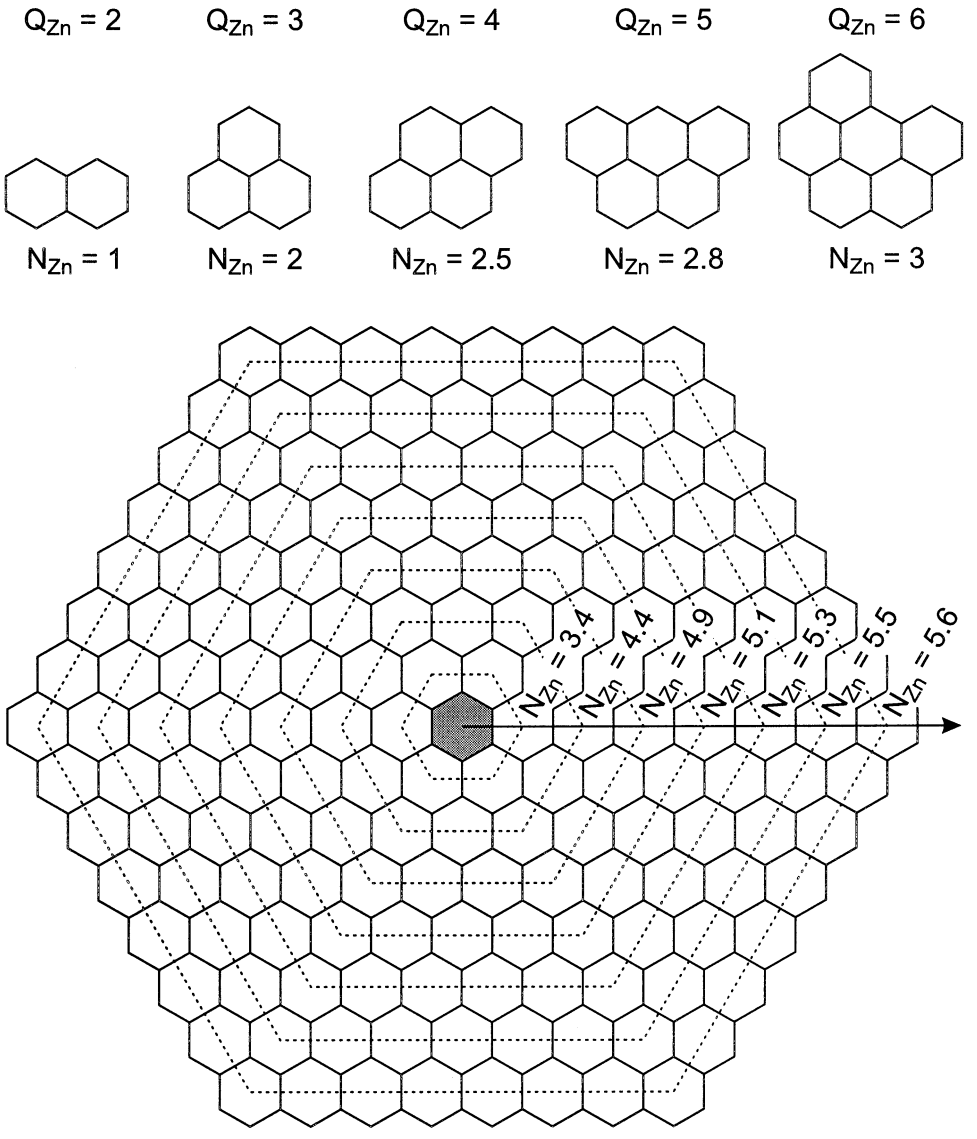

Fig. 11. Average number of nearest Zn atomic neighbors (N_{Zn}) in octahedral sheet as a function of its dimension (Q_{Zn}).

not only explains the relatively high $N_{Si}^{35°}$ value, but also accounts for the observed Si uptake (169 μmol g^{-1} at t = 9 h; Fig. 3d). The ratio of Si to Zn neighboring atoms in these nuclei, as estimated from the $N_{Si}^{35°}/N_{Zn}^{35°}$ ratio, equals (1.5 ± 0.4)/(3.8 ± 0.2) = 0.39 ± 0.10. This value does not match the ratio for a TOT clay structure ($N_{Si}^{35°}/N_{Zn}^{35°}$ = 4/6 ≈ 0.67), but is compatible within uncertainties to that for a TO structure ($N_{Si}^{35°}/N_{Zn}^{35°}$ = 2/6 ≈ 0.33). Therefore, Zn clay nuclei may consist of either stoichiometric TO particles, of Si-depleted TOT particles, or of a mixture of TO and TOT particles (Fig. 12b–d).

The mean size of Zn octahedral sheets much increased from t = 9 h (Q_{Zn} ≈ 20) to t = 120 h (Q_{Zn} ≥ 200). At t = 120 h, the number of in-plane Zn (6 ± 0.4) and out-of-plane Si (3.6 ± 0.4) surrounding Zn are consistent with, but do not prove, the formation of stoichoimetric TOT phyllosilicate because of the uncertainty on $N_j^{35°}$. Further insight on the structure of Zn clay particles can be obtained from elemental Si/Zn ratios, either experimental (1.09 ± 0.08) or corrected for hectorite dissolution (1.14 ± 0.09; Fig. 3d), which are intermediate between TO and TOT stoichiometry. Therefore, among the three structural possibilities envisaged at t = 9 h, two remain for this sample: a mixture of stoichiometric TO and TOT particles (Fig. 12e; Brindley and Hang, 1973), or Si-depleted defective TOT particles (Fig. 12f; Drits and Tchoubar, 1990). Further studies involving analytical electron microscopy may help to solve these alternatives. Note that the formation of nonstoichiometric TOT Zn layers or a mixture of TOT and TO Zn layers is expected to weaken the cohesion forces between hectorite particles. This can explain the decrease in texture strength of self-supporting films with increasing amounts of sorbed Zn.

4.1.3. Growth mechanism of Zn clay particles at high $[Si]_{aq}$

Simultaneous uptake of Zn and Si for t ≥ 9 h suggests that phyllosilicate growth from solute species is a cooperative pro-

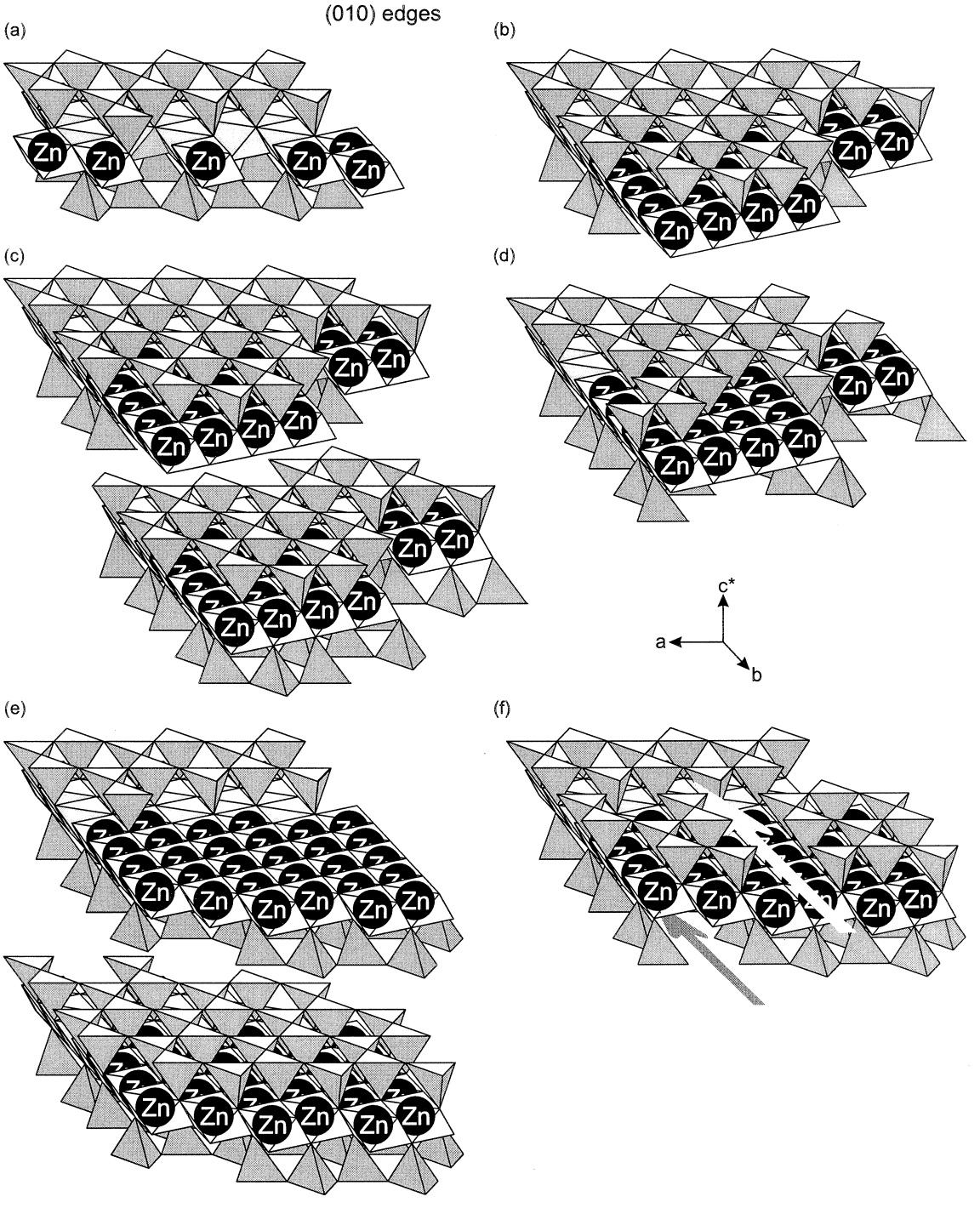

Fig. 12. Structural models for the Zn environment in sorption samples. (a) Structural model at $[Si]_{aq}$ ~30–60 μM, and 96 h of reaction time (H30_Zn_96h). Small Zn polymers formed at the layer edges of hectorite in structural continuity with (Mg, Li) octahedral sheets. (b,c,d) Possible structural models at $[Si]_{aq}$ ~530 μM and 9 h of reaction time (H30_SiZn_9h). Zn cations form octahedral sheets in continuity with (Mg, Li) octahedral sheets and bridged to Si tetrahedral sheets at the layer edges of hectorite. The nuclei of Zn hydrous silicate have either (c) a TO structure, (d) TO and TOT mixed structures, or (e) a TOT structure with highly defective tetrahedral sheets. (e,f) Possible structural models at $[Si]_{aq}$ ~530 μM and 120 h of reaction time (H30_SiZn_120h). (e) Mixture of TO and TOT nuclei. (f) TOT layers with defective tetrahedral sheets. In all cases, the Zn clay domains are epitaxially grown on the edges of hectorite layers.

cess, with Zn and Si sheets growing at about the same rate. These growth reactions can be written respectively for TO and TOT Zn-phyllosilicates:

$$3\,Zn^{2+} + 2\,Si(OH)_4 + H_2O = Zn_3Si_2O_5(OH)_4 + 6\,H^+ \quad (5)$$

$$3\,Zn^{2+} + 4\,Si(OH)_4 = Zn_3Si_4O_{10}(OH)_2 + 6\,H^+ + 4\,H_2O \quad (6)$$

Precipitation of solution species decreases the solution supersaturation, as reflected by the decrease of the IAP values, which are classically written for the reverse reactions of Eqn. 5 and 6:

$$IAP_{TO} = \frac{(Zn^{2+})^3\,(Si(OH)_4)^2}{(H^+)^6} \quad (7)$$

and

$$IAP_{TOT} = \frac{(Zn^{2+})^3\,(Si(OH)_4)^4}{(H^+)^6} \quad (8)$$

Assuming an ideal TOT composition, IAP_{TOT} decreases from $\sim 10^{8.5\,\pm\,5.9}$ at t = 3 h to $\sim 10^{16\,\pm\,1}$ at t = 120 h. The value obtained at t = 120 h can be considered as an upper limit for the solubility value of TOT Zn-phyllosilicate. Note that this limit is consistent with the previous theoretical estimate of this solubility, $K_{Znclay} = 10^{8.5\,\pm\,5.9}$ (Manceau et al., 2000).

The increase in amount of sorbed Zn (from 227 μmol g^{-1} at t = 9 h to 725 μmol g^{-1} at t = 120 h) and the average size of Zn-phyllosilicate nuclei at t = 9 h ($Q_{Zn} \approx 20$) would have implied that $Q_{Zn} \approx 60$ ($N_{Zn}^{35°} \approx 5$) at t = 120 h if all particles had grown at similar rates. A much higher experimental Q_{Zn} value ($Q_{Zn} \geq 200$) was observed, which could be explained either by the growth of some nuclei and the concomitant dissolution of others by Ostwald ripening (Eberl et al., 1998), or by the coalescence of adjacent particles during growth. On the one hand, estimation of the critical size below which dissolution occurs requires precise knowledge of the solubility constant and the surface free energy of these nanosized particles. Neither of these parameters has been determined experimentally, precluding any estimation of the nuclei critical size. Therefore, the occurrence of Ostwald ripening cannot be assessed quantitatively. On the other hand, Zn clay nuclei growing at hectorite edges may coalesce if they are not too far apart. At t = 9 h, the amount of these nuclei, estimated from sorbed Zn (227 μmol g^{-1}) and from $Q_{Zn} \approx 20$, is 11 μmol g^{-1}. Contrasting this value to the number of hectorite edge sorption sites ($\sim$92 μmol g^{-1}; Schlegel et al., 1999b) shows that about one out of nine edge surface sites have attached Zn nuclei, resulting in an average internuclei distance ($\approx$ 25 Å) > the average Zn clay nuclei diameter of $\approx$ 15 Å. At t = 120 h, $Q_{Zn} \approx 60$ yields an average nuclei diameter of 30 Å, greater than the average internuclei distance at 9 h. Therefore, adjacent nuclei could have merged and formed larger particles on growth. Furthermore, Zn nuclei likely were not distributed at random on hectorite edges, but presumably were clustered in the vicinity of edge defects, thereby reducing distances between the growing particles in these clusters. In conclusion, coalescence of adjacent nuclei is a probable mechanism that can explain, at least semiquantitatively, the higher than expected Q_{Zn} value at t = 120 h.

4.2. Application to Field Studies

The rapid formation of Zn phyllosilicate at near-neutral pH and Si concentration, representative of natural solutions, suggests that this mechanism of Zn immobilization is plausible in terrestrial systems. Indeed, Zn K-edge P-EXAFS spectra recorded on self-supporting films of soil clay fractions from smelter-contaminated soils were markedly anisotropic and resembled those obtained in the present study (Manceau et al., 2000). This suggested that Zn clay particles nucleated and grew epitaxially on existing soil phyllosilicates, such as smectites, illites, and chlorites, because clay particles formed by homogeneous precipitation would likely be oriented randomly (Decarreau, 1980).

The results presented in this study also provide some insight on the formation mechanism of (Ni, Mg) phyllosilicates, called garnierites, found as crack-filling material in weathering profiles of ultrabasic rocks (Brindley and Hang, 1973; Pelletier, 1983). Garnierites are believed to result from the coprecipitation of Ni, Mg, and Si released upon weathering of rock-forming minerals (Pelletier, 1983). Manceau and Calas (1985, 1986) showed that Ni is not substituted randomly for Mg in the TO (serpentine) and TOT (kerolite) phyllosilicates from garnierites, but is systematically segregated within Ni-rich domains even for Ni/(Ni + Mg) elemental ratios as low as 0.07. Owing to the similar affinity of Zn and Ni for a phyllosilicate structure (Decarreau, 1981, 1985), the heteronucleation and growth mechanism identified here for Zn can be transposed to Ni and may explain the existence of Ni-rich domains in garnierites.

5. CONCLUDING REMARKS

The present study highlights the impact of $[Si]_{aq}$ on the sorption mechanism of Zn on smectite minerals at pH 7.30 and Zn concentrations undersaturated with respect to both hydroxide and ZnO oxide phases. At low $[Si]_{aq}$ ($\sim$30 to 60 μM; $\sim$ 4 ppm SiO_2), only Zn polymers of small mean size formed at layer edges of hectorite, indicating that the hectorite surface cannot promote the precipitation of large Zn hydroxide layers and Zn oxide in undersaturated conditions. In contrast, the nucleation and extensive growth of Zn phyllosilicate was observed after only 5 d at $[Si]_{aq}$ $\sim$530 μM ($\sim$32 ppm SiO_2), i.e., at concentrations relevant to field conditions. Therefore, dissolved Si undoubtedly exerts a key role in the fate of Zn and chemically similar cations in natural systems and should not be omitted in laboratory systems designed to simulate natural conditions.

Acknowledgments— K. L. Nagy is gratefully acknowledged for her scientific comments. The authors thank G. Sposito and three anonymous reviewers for their constructive comments on the manuscript. J. J. Menthonnex, Y. Soldo, O. Prost, and O. Ulrich are thanked for their assistance in the collection of EXAFS spectra, and the ESRF is acknowledged for the provision of beamtime.

Associate editor: G. Sposito

REFERENCES

Aberdam D. (1998) SEDEM, a software package for EXAFS data extraction and modeling. *J. Synchrotron Rad.* **5,** 1287–1297.

Anderson S. J. and Sposito G. (1991) Cesium-adsorption method for

measuring accessible structural surface charge. *Soil Sci. Soc. Am. J.* **55,** 1569–1576.
Baes C. F. J. and Mesmer R. E. (1976) *The Hydrolysis of Cations.*Wiley, New York.
Banfield J. F., Jones B. F., and Veblen D. R. (1991) An AEM-TEM study of weathering and diagenesis, Albert Lake, Oregon: 1. Weathering reactions in the volcanics. *Geochim. Cosmochim. Acta* **55,** 2781–2793.
Brindley G. W. and Hang P. T. (1973) The nature of garnierite. I. Structures, chemical compositions and color characteristics. *Clay Miner.* **21,** 27–40.
Charlet L. and Manceau A. (1994) Evidence for the neoformation of clays upon sorption of Co(II) and Ni(II) on silicates. *Geochim. Cosmochim. Acta* **58,** 2577–2782.
Davies S. N. and De Wiest R. C. M. (1966) *Hydrogeology.* Wiley, New York.
Davis J. A., Coston J. A., Kent D. B., and Fuller C. C. (1998) Application of the surface complexation concept to complex mineral assemblages. *Environ. Sci. Technol.* **32,** 2820–2828.
Decarreau A. (1980) Cristallogenèse expérimentale des smectites magnésiennes: hectorite, stevensite. *Bull. Soc. Franç. Minér. Crist.* **103,** 579–590.
Decarreau A. (1981) Mesure expérimentale des coefficients de partage solide/solution pour les éléments de transition A^{2+} dans les smectites magnésiennes (A= Ni, Co, Zn, Fe, Cu, Mn). *C. R. Acad. Sc. Paris* **292,** 459–462.
Decarreau A. (1985) Partitioning of divalent transition elements between octahedral sheets of trioctahedral smectites and water. *Geochim. Cosmochim. Acta* **49,** 1537–1544.
Drever J. I. (1997) *The Geochemistry of Natural Waters.* Prentice Hall, Upper Saddle River, NJ.
Drits V. A. and Tchoubar C. (1990) *X-ray Diffraction by Disordered Lamellar Structures.* Springer Verlag, Berlin.
Eberl D. D., Drits V. A., and Srodon J. (1998) Deducing growth mechanisms for minerals from the shapes of crystal size distributions. *Am. J. Sci.* **298,** 499–533.
Espinose de la Caillerie J.-B., Kermarec M., and Clause O. (1995) ^{29}Si NMR observation of an aqueous magnesium silicate formed during impregnation of silica with Mg(II) in aqueous solution. *J. Phys. Chem.* **99,** 17273–17281.
Farquhar M. L., Charnock J. M., England K. E. R., and Vaughan D. J. (1996) Adsorption of Cu(II) on the (0001) plane of mica: A REFLEXAFS and XPS study. *J. Colloid Interf. Sci.* **177,** 561–567.
Fortin D., Ferris F. G., and Beveridge T. G. (1997) Surface-mediated mineral development by bacteria. In *Interactions Between Microbes and Minerals. Reviews in Mineralogy* (ed. J. F. Banfield and K. H. Nealson), Vol. 35, pp. 161–180, Mineralogical Society of America, Washington, DC.
Harder H. (1977) Clay mineral formation under lateritic weathering conditions. *Clay Miner.* **12,** 281–288.
Hazemann J. -L., Nayouf K., and Debergevin F. (1995) Modelization by finite-elements of sagittal focusing. *Nucl. Instrum. Methods* **B97,** 547–550.
Iler R. K. (1979) *The Chemistry of Silica.* Wiley, New York.
Kuzmin A., Obst S., and Purans J. (1997) X-ray absorption spectroscopy and molecular dynamics studies of Zn^{2+} hydration in aqueous solutions. *J. Phys. Condens. Matter* **9,** 10065–10078.
Manceau A. and Calas G. (1985) Heterogeneous distribution of nickel in hydrous silicates from New Caledonia ore deposits. *Am. Mineral.* **70,** 549–558.
Manceau A. and Calas G. (1986) Nickel-bearing clay minerals: II. Intracrystalline distribution of nickel: An X-ray absorption study. *Clay Miner.* **21,** 341–360.
Manceau A. and Combes J.-M. (1988) Structure of Mn and Fe oxides and oxyhydroxides: A topological approach by EXAFS. *Phys. Chem. Miner.* **15,** 283–295.
Manceau A. and Schlegel M. L. (2001) Texture effect on polarized EXAFS amplitude. *Phys. Chem. Miner.* **28,** 52–56.
Manceau A., Bonnin D., Stone W. E. E., and Sanz J. (1990) Distribution of Fe in the octahedral sheet of trioctahedral micas by polarized EXAFS. Comparison with NMR results. *Phys. Chem. Miner.* **17,** 363–370.
Manceau A., Chateigner D., and Gates W. P. (1998) Polarized EXAFS, distance-valence least-squares modeling (DVLS) and quantitative texture analysis approaches to the structural refinement of Garfield nontronite. *Phys. Chem. Miner.* **25,** 347–365.
Manceau A., Schlegel M., Nagy K. L., and Charlet L. (1999a) Evidence for the formation of trioctahedral clay upon sorption of Co^{2+} on quartz. *J. Colloid Interf. Sci.* **220,** 181–197.
Manceau A., Schlegel M. L., Chateigner D., Lanson B., Bartoli C., and Gates W. P. (1999b) Application of polarized EXAFS to fine-grained layered minerals. In *Synchrotron X-ray Methods in Clay Science*. (ed. D. G. Schulze, J. W. Stucki, and P. M. Bertsch), pp. 69–114. Clay Mineral Society of America, Boulder, CO.
Manceau A., Lanson B., Schlegel M. L., Hargé J.-C., Musso M., Hazemann J.-L., Chateigner D., and Lamble G. M. (2000) Quantitative Zn speciation in smelter-contaminated soils by EXAFS spectroscopy. *Am. J. Sci.* **300,** 289–343.
Nagy K. L., Cygan R. T., Hanchar J. M., and Sturchio N. C. (1999) Gibbsite growth kinetics on gibbsite, kaolinite, and muscovite substrates: Atomic force microscopy evidence for epitaxy and an assessment of reactive surface area. *Geochim. Cosmochim. Acta* **63,** 2337–2351.
O'Day P. A., Parks G. A., and Brown G. E., Jr. (1994a) Molecular structure and binding of Cobalt(II) surface complexes on kaolinite from X-ray absorption spectroscopy. *Clay. Clay Miner.* **42,** 337–355.
O'Day P. A., Rehr J. J., Zabinsky S. I., and Brown G. E. Jr. (1994b) Extended X-ray absorption fine structure (EXAFS) analysis of disorder and multiple-scattering in complex crystalline solids. *J. Am. Chem. Soc.* **116,** 2938–2949.
O'Day P. A., Chisholm-Brause C. J., Towle S. N., Parks G. A., and Brown G. E. Jr. (1996) X-ray absorption spectroscopy of Co(II) sorption complexes on quartz (α -SiO_2) and rutile (TiO_2). *Geochim. Cosmochim. Acta* **60,** 2515–2532.
Papelis C. and Hayes K. F. (1996) Distinguishing between interlayer and external sorption sites of clay minerals using X-ray absorption spectroscopy. *Colloid. Surface A* **107,** 89–96.
Pelletier B. (1983) Localisation du nickel dans les minerais 'garniéritiques' de la Nouvelle Calédonie. *Sci. Géol. Mém.* **73,** 173–183.
Rayner J. H. and Brown G. (1973) The crystal structure of talc. *Clay. Clay Miner.* **21,** 103–114.
Rehr J. J., Albers R. C., and Zabinsky S. I. (1992) High-order multiple-scattering calculations of X-ray absorption fine structure. *Phys. Rev. Lett.* **69,** 3397–3400.
Righi D. and Meunier A. (1995) Origin of clays by rock weathering and soil formation. In *Origin and Mineralogy of Clays* (ed. B. Velde), pp. 43–161, Springer, Berlin.
Rimstidt J. D. (1997) Quartz solubility at low temperatures. *Geochim. Cosmochim. Acta* **61,** 2553–2558.
Sarret G., Manceau A., Spadini L., Roux J. C., Hazemann J.-L., Soldo Y., Eybert-Berard L., and Menthonnex J.-J. (1998) Structural determination of Zn and Pb binding sites in *Penicillium chrysogenum* cell walls by EXAFS spectroscopy. *Environ. Sci. Technol.* **32,** 1648–1655.
Scheidegger A. M., Lamble G. M., and Sparks D. L. (1996) Investigation of Ni adsorption on pyrophyllite: an XAFS study. *Environ. Sci. Technol.* **30,** 548–554.
Scheidegger A. M., Lamble G. M., and Sparks D. L. (1997) Spectroscopic evidence for the formation of mixed-cation hydroxide phases upon metal sorption on clay and aluminium oxides. *J. Colloid Interf. Sci.* **186,** 118–128.
Scheidegger A. M., Strawn D. G., Lamble G. M., and Sparks D. L. (1998) The kinetics of mixed Ni-Al hydroxide formation on clay and aluminium oxide minerals: A time-resolved XAFS study. *Geochim. Cosmochim. Acta* **62,** 2233–2245.
Schlegel M. L., Manceau A., Chateigner D., and Charlet L. (1999a) Sorption of metal ions on clay minerals. I. Polarized EXAFS evidence for the adsorption of cobalt on the edges of hectorite particles. *J. Colloid Interf. Sci.* **215,** 140–158.
Schlegel M. L., Charlet L., and Manceau A. (1999b) Sorption of metal ions on clay minerals. II. Mechanism of Co sorption on hectorite at

high and low ionic strength, and impact on the sorbent stability. *J. Colloid Interf. Sci.* **220,** 392–405.
Schlegel M. L., Manceau A., Hazemann J.-L., and Charlet L. (2001) Adsorption mechanism of Zn on hectorite as a function of time, pH, and ionic strength. *Am. J. Sci.*, in press.
Stern E. A. (1993) Number of relevant independent points in X-ray absorption fine structure spectra. *Phys. Rev. B.* **48,** 9825–9827.
Stumm W. (1992) *Chemistry of the Solid–Water Interface.* Wiley, New York.
Stumm W. and Morgan J. J. (1996) *Aquatic Chemistry*, 2nd Ed., Wiley, New York.
Taylor J. R. (1997) *An Introduction to Error Analysis.* University Science Books, Sausalito, CA.
Teo B. K. (1986) *EXAFS: Basic Principles and Data Analysis.* Springer-Verlag, Berlin.
Towle S. N., Bargar J. R., Brown, Jr. G. E., and Parks G. A. (1997) Surface precipitation of $Co(II)_{(aq)}$ on Al_2O_3. *J. Colloid Interf. Sci.* **187,** 62–82.